
# NAVAL POSTGRADUATE SCHOOL

**MONTEREY, CALIFORNIA**

# THESIS

**INCREASING PERFORMANCE OF THE RQ-20 PUMA WITH PHOTOVOLTAIC CELLS**

by

Christopher Perez

September 2018

| | |
|---|---|
| Thesis Advisor: | Sherif N. Michael |
| Second Reader: | James Calusdian |

THIS PAGE INTENTIONALLY LEFT BLANK

| REPORT DOCUMENTATION PAGE | | | *Form Approved OMB No. 0704-0188* |
|---|---|---|---|



| **1. AGENCY USE ONLY** *(Leave blank)* | **2. REPORT DATE** September 2018 | **3. REPORT TYPE AND DATES COVERED** Master's thesis |
|---|---|---|

| **4. TITLE AND SUBTITLE** INCREASING PERFORMANCE OF THE RQ-20 PUMA WITH PHOTOVOLTAIC CELLS | **5. FUNDING NUMBERS** |
|---|---|
| **6. AUTHOR(S)** Christopher Perez | |
| **7. PERFORMING ORGANIZATION NAME(S) AND ADDRESS(ES)** Naval Postgraduate School Monterey, CA 93943-5000 | **8. PERFORMING ORGANIZATION REPORT NUMBER** |
| **9. SPONSORING / MONITORING AGENCY NAME(S) AND ADDRESS(ES)** N/A | **10. SPONSORING / MONITORING AGENCY REPORT NUMBER** |

**11. SUPPLEMENTARY NOTES** The views expressed in this thesis are those of the author and do not reflect the official policy or position of the Department of Defense or the U.S. Government.

| **12a. DISTRIBUTION / AVAILABILITY STATEMENT** Approved for public release. Distribution is unlimited. | **12b. DISTRIBUTION CODE** A |
|---|---|

**13. ABSTRACT (maximum 200 words)**

In this research, we focus on quantifying the flight endurance gains possible for a variety of flight profiles and environments by adding commercially available thin film photovoltaic cells and power electronics hardware to the RQ-20 Puma small unmanned aerial vehicle. We use a combination of precise aircraft sub-component power utilization measurements, in-flight performance data, and precise calculations of solar azimuth, elevation, and intensity. The result of our analysis is a novel computer model of the aircraft and photovoltaic system that accounts for geographic location, altitude, and time of year, and then predicts minute-by-minute battery charge over the course of a dynamic flight profile. We conclude that substantial flight endurance gains are possible in the most favorable environments, and modest but worthwhile gains are even possible with little sunlight. Based on our findings and a favorable cost-benefit analysis, we recommend that the Navy and Marine Corps pursue full-flight testing in support of fielding this technology across the RQ-20 inventory.

| **14. SUBJECT TERMS** RQ-20 Puma, flexible photovoltaic cells, CIGS, flight endurance | **15. NUMBER OF PAGES** 99 |
|---|---|
| | **16. PRICE CODE** |

| **17. SECURITY CLASSIFICATION OF REPORT** | **18. SECURITY CLASSIFICATION OF THIS PAGE** | **19. SECURITY CLASSIFICATION OF ABSTRACT** | **20. LIMITATION OF ABSTRACT** |
|---|---|---|---|
| Unclassified | Unclassified | Unclassified | UU |

NSN 7540-01-280-5500 Standard Form 298 (Rev. 2-89) Prescribed by ANSI Std. 239-18

THIS PAGE INTENTIONALLY LEFT BLANK

**Approved for public release. Distribution is unlimited.**

# INCREASING PERFORMANCE OF THE RQ-20 PUMA WITH PHOTOVOLTAIC CELLS

Christopher Perez
Major, United States Marine Corps
BS, U.S. Naval Academy, 2007

Submitted in partial fulfillment of the
requirements for the degree of

**MASTER OF SCIENCE IN ELECTRICAL ENGINEERING**

from the

**NAVAL POSTGRADUATE SCHOOL**
**September 2018**

Approved by: Sherif N. Michael
Advisor

James Calusdian
Second Reader

Clark Robertson
Chair, Department of Electrical and Computer Engineering

THIS PAGE INTENTIONALLY LEFT BLANK

# ABSTRACT

In this research, we focus on quantifying the flight endurance gains possible for a variety of flight profiles and environments by adding commercially available thin film photovoltaic cells and power electronics hardware to the RQ-20 Puma small unmanned aerial vehicle. We use a combination of precise aircraft sub-component power utilization measurements, in-flight performance data, and precise calculations of solar azimuth, elevation, and intensity. The result of our analysis is a novel computer model of the aircraft and photovoltaic system that accounts for geographic location, altitude, and time of year, and then predicts minute-by-minute battery charge over the course of a dynamic flight profile. We conclude that substantial flight endurance gains are possible in the most favorable environments, and modest but worthwhile gains are even possible with little sunlight. Based on our findings and a favorable cost-benefit analysis, we recommend that the Navy and Marine Corps pursue full-flight testing in support of fielding this technology across the RQ-20 inventory.

THIS PAGE INTENTIONALLY LEFT BLANK

# TABLE OF CONTENTS

# LIST OF FIGURES

# LIST OF TABLES

# LIST OF ACRONYMS AND ABBREVIATIONS

| | |
|---|---|
| AE | all environment |
| AOA | angle of attack |
| AOB | angle of bank |
| AGL | above ground level |
| CIGS | Copper Indium Gallium Selenide |
| DoD | Department of Defense |
| EO | electro-optical |
| ERI | Evolving Resources Inc. |
| IAS | indicated airspeed |
| IR | infrared |
| MPP | maximum-power point |
| MPPT | maximum-power point tracking |
| MSL | mean sea level |
| NPS | Naval Postgraduate School |
| PV | photovoltaic |
| SUAS | small unmanned aerial system |
| TFPV | thin film photovoltaic |
| TTP | tactics, techniques, and procedures |
| UAV | unmanned aerial vehicle |
| USMC | United States Marine Corps (text) |
| VO | vehicle operator |

THIS PAGE INTENTIONALLY LEFT BLANK

# ACKNOWLEDGMENTS

We would like to thank Albert Gomez, Richard Gomez, Danny Ensenat, and Jose Guerrero from Evolving Resources Inc. for their assistance with access and technical assistance in gathering performance data from the RQ-20 Puma. We are also appreciative of the assistance from Ernie Cardenas and Henry Estorga from TALSA-West for allowing observation of flight training and maneuvers, and assistance with gathering flight data.

THIS PAGE INTENTIONALLY LEFT BLANK

# I. INTRODUCTION

## A. BACKGROUND

Small unmanned aerial systems (SUAS) are a category of unmanned aerial vehicle (UAV) that generally utilize battery power, operate with an electric motor, weigh 2–20 kg, fly up to 5000 ft. above ground level (AGL) for a combat radius of 25–50 km with 1–3 hr flight endurance and need only one or two individuals for operation and maintenance. Already widely utilized by the U.S. military and becoming even more commonplace among other defense agencies [1], SUAS offer their users an ability to see—often covertly—objects and activity from a relatively safe distance that otherwise would not be possible from the ground. They cover a surveillance and reconnaissance requirement that would otherwise only be achievable through employment of manned aircraft or national assets at either much higher cost or physical risk to aircrew.

Due to their demonstrated usefulness, relative low cost, and portability, SUAS are in high demand by warfighters and commanders alike. Recognizing these benefits, the USMC in particular is seeking to expand the capabilities and inventory of SUAS to meet burgeoning requirements for these systems [2]. The RQ-20 Puma is one such system in widespread use by the USMC and other government entities today. This specific system will remain in service for many more years [1] and is representative of the higher-end capability set of SUAS.

An inherent limitation of such systems is their limited flight endurance and payload capacity because of their small size and tradeoffs between cost, complexity, and portability. The endurance problem is aggravated by the fact that the small units employing these systems are often operating from an austere environment with limited supplies and at the tail end of a long supply chain. In order to provide persistent SUAS surveillance, users must maintain multiple systems and numerous batteries to provide overlapping coverage on a battlefield. The recovery, repair, preflight, and launch cycle consumes additional time, resources, and even prohibits some preferred employment options [3], such as when a covert reconnaissance unit must maintain concealment.

The integration of relatively recent advancements in thin and flexible solar cell technology onto SUAS offers the potential to mitigate some of these endurance and payload limitations. Flexible solar cells are already a familiar technology being utilized today by forces in applications like solar blankets [4] to recharge batteries in austere environments. The Department of Defense (DoD) and USMC are additionally making a concerted effort across the enterprise to emphasize renewable energy solutions to reduce the demand for resupply. Strategic requirements captured in a comprehensive review conducted by the Marine Corps Expeditionary Energy Office forecast a future operational environment supported by renewable-powered UAS [5].

## B. OBJECTIVE

In this project, we seek to capitalize on previous research that demonstrated the feasibility of using photovoltaic (PV) technology to address one of the persistent limitations of existing SUAS. In this research, we will specifically focus on quantifying the flight endurance gains that are possible in a variety of flight profiles and environments with the addition of thin film photovoltaic (TFPV) cells to the upper wing surface of the RQ-20 Puma.

In addition to quantifying these performance gains relative to existing methods of aircraft employment, in this research we will identify possible changes to tactics, techniques, and procedures (TTPs) that would be beneficial to fully capitalize on a PV-equipped SUAS. Our proposed system will utilize commercially available hardware so that expected costs can be considered. A cost-benefit analysis will determine if the technology can be justified for immediate incorporation to current platforms or to inform the next generation of research and development. These conclusions have immediate impact on a platform widely employed by the USMC and used by other military branches and government agencies and are especially relevant to operational scenarios that call for greater time on station or payload capacity that are presently constrained by time on station or payload weight limits.

## C. RELATED WORK

Previous NPS research demonstrated the feasibility of incorporating thin film photovoltaic cells to the wings of SUAS to increase performance. In 2009, W. Hurd [6] demonstrated this technology on a commercial remote controlled airplane similar in size to the RQ-11 Raven using flexible G2 Thin Film Strings produced by Global Solar Energy. Between 2010 and 2014, J. Coba [7], C. Chin [8], C. Gromadski [4], and S. Carey [9] evaluated this PV technology on the Raven, a SUAS roughly one-third the weight and half the wingspan of the RQ-20 Puma utilizing the same G2 solar cells. In 2017, M. Lai expanded this line of research by incorporating a new line of high-efficiency TFPV cells from Global Solar. Installing these TFPV cells on a Puma wing, Lai's research measured the actual power output from the solar array and broadly estimated power consumption and environmental conditions, concluding that indefinite daylight operations were possible for the Puma [10].

Other NPS research by N. Camacho [11] in 2014 integrated C60 monocrystalline silicon solar cells from Sun Power Corp. onto an autonomous glider to power onboard electronics that enabled long-duration autonomous soaring flight. A similar line of research by the Naval Research Lab [12] developed methods for optimizing aircraft flight attitude and maneuvers for a small, PV equipped, glider-type aircraft.

## D. APPROACH

To reach the project objectives, in this research we first seek to gather and process precise data on sub-component power requirements for the RQ-20 Puma using bench tests in a controlled laboratory environment. Then, utilizing live, in-flight measurements, additional detailed data will be gathered on key flight performance parameters seen in typical mission profiles. In parallel with the data collection, we will also compile and validate precise mathematical models of solar characteristics to enable accurate prediction of power generation from a dynamic airborne PV array over the course of a typical mission profile. After incorporating previously researched power electronics system configurations, we will calculate the performance gains expected for the Puma across a variety of environments in the proposed TFPV configuration.

THIS PAGE INTENTIONALLY LEFT BLANK

# II. FUNDAMENTALS

This chapter begins with a review of the selected SUAS, some of its selected characteristics and its performance. We briefly review photovoltaic technology as it applies to our application and the specific type of cells chosen. Next, the process of estimating the amount of solar irradiance reaching the surface of the earth is explored in some detail along with a methodology for applying this to the array on our aircraft wing. Lastly, we review the other power electronics components required for the operation of this system to translate power from the solar array to the aircraft and its battery.

## A. RQ-20 PUMA

### 1. Mission and Operation

The RQ-20 Puma AE (all environment) is one of the largest and most capable SUAS of its class, suitable for day and night operations over land or water. The aircraft is lightweight and portable with relatively long flight endurance and precision GPS navigation capabilities. The system can provide overhead surveillance with gimbaled electro-optical (EO) or infrared (IR) payloads. Typically hand-launched, the aircraft can also be launched from moving trucks or ships and is recovered through a deep-stall landing on either land or water [13].

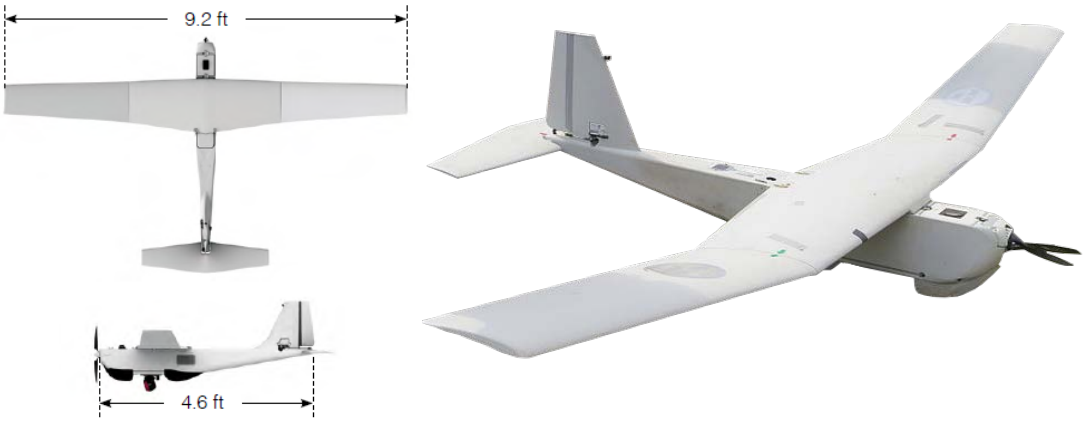


Figure 1. RQ-20 Puma. Source [13] and [14].

A two-person team typically employs the aircraft: a “vehicle operator” who controls the aircraft and a “mission operator” who operates the sensor payload. After launch, several flight modes can be selected, to include manual and fully autonomous flight modes along pre-designated and dynamically adjustable flight plans [15].

## 2. Performance Characteristics and Limits

Though capable of flight up to several thousand feet and up to 20 km away, aircraft are typically operated less than a thousand feet above the ground for greater sensor resolution and within a radius of several kilometers [3]. Summarized in Table 1, the three-hour endurance, while longer than most SUAS, effectively limits the distance at which an operator can employ the system due to the time required to fly long distances at a typical 23 knot cruising speed.

Table 1. RQ-20B Puma specifications. Adapted from [13].

| Parameter | Specification | Parameter | Specification | Parameter | Specification |
|---|---|---|---|---|---|
| Wingspan | 9.2 ft (2.8 m) | Weight | 14 lbs | Endurance | 3+ hrs |
| Wing Area | 7160 $cm^2$ | Speed | 25-45 kts | Operating Altitude | 500 - 12,500 ft |
| Length | 4.6 ft (1.4 m) | Range | 20 km | | |

For recovery, the aircraft employs a “deep-stall landing” technique, which brings the aircraft close to the ground at a slow speed before pitching up to a stalled attitude. This approach allows the aircraft to “land” nearly vertically in a confined area, impacting the bottom of the fuselage. Fittings are designed to allow the wings to breakaway and areas of the fuselage are reinforced to improve durability on impact; however, landings occasionally cause damage. Users are trained to complete minor repairs between flights; more extensive depot-level repairs are necessary periodically to repair inevitable cracks and composite damage after a number of flights.

## 3. Payloads

Two primary payload options currently exist for the Puma. The standard i25 payload is present on most current aircraft and was tested in this research. A newer and

more capable i45 payload is in limited use, primarily by special operations forces. Both payloads provide an EO/IR camera with an integrated IR illuminator. A notable feature of the standard Puma payload is the stabilized gimbaled sensor, allowing for pan, tilt, and zoom in nearly any direction below the aircraft. This feature is not present on most other SUAS of the class, which generally use fixed cameras and often lack optical zoom and stabilization. Another payload option used less often provides for simple electronic-warfare capabilities, to include interception of common push-to-talk radio frequencies.

## B. PHOTOVOLTAIC TECHNOLOGY AND EFFICIENCY

### 1. Semiconductors and P-N Junction

The basis of all PV cells is a P-N junction of crystalline semiconductor material that acts similar to a reverse-biased diode. A so-called “n-type” material doped to have a higher concentration of electrons is layered with a “p-type” material doped to have a high concentration of “holes” (a temporary positive charge resulting from a displaced or “missing” electron around an atom). At the junction between the two materials, a diffusion of electrons from the n-layer to the p-layer forms a depletion region where electrons and holes have recombined on either side of the junction. The difference in charge that results from this diffusion creates an electric field of charged ions in the semiconductor material.

### 2. Band Gap and Photovoltaic Effect

The band gap refers to the potential of the electric field created by the diffusion of electrons in the depletion region of the solar cell. When an electron in the valence band of one of the semiconductor atoms receives sufficient energy from a photon of solar radiation, the electron is freed from its parent atom and is attracted by the potential of the band gap to jump to the nearby conduction band. The hole created by the displaced election is in-turn filled by another electron from an adjacent atom (which also produces a new hole), creating an electric current through the semiconductor material [16]. The photovoltaic effect is the name given to this physical process through which the PV cell converts sunlight into electrical energy.

## 3. Constructing the PV Cell

To adapt the p-n junction of semiconductor material to form a solar cell and harvest the electric current generated, metal contacts are added to either side of the semiconductor. The metal contacts are connected to adjacent cells and eventually to a load to provide a path for the current from the PV cell to power the load. To improve performance, an anti-reflection layer and or a precisely textured surface may be also added on the top of the absorption layer of the p-n junction to increase the amount of light that passes through and into the semiconductor.

## 4. CIGS PV Cells

Copper indium gallium selenide (CIGS) is a special type of semiconductor compound initially developed to be a lower-cost alternative to traditional silicon PV cells. CIGS uses the properties of its component materials, layered with other compounds as shown in Figure 2, to achieve a high solar efficiency in a thin film with a band gap of 1.0 to 1.7 eV. In contrast to traditional silicon-based PV materials, CIGS have very strong absorption characteristics and can achieve their performance even from a very thin layer. CIGS are, therefore, easily incorporated on a flexible substrate, making it ideal for cells that will be mounted to a curved surface like the airfoil of an aircraft wing. In general, CIGS PV cells are the most efficient type of flexible thin-film cells produced [8].

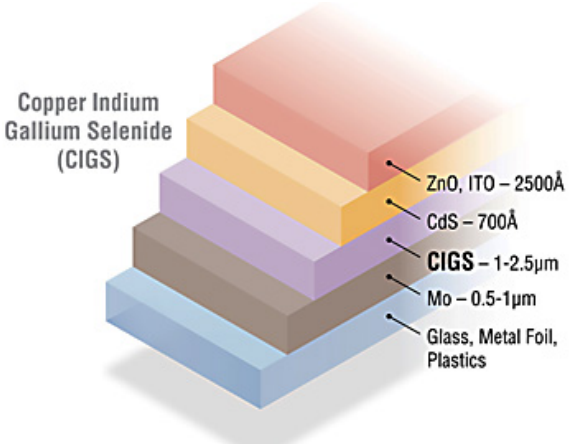


Figure 2. Composition of CIGS PV cell. Source [17].

## 5. Efficiency and Factors for Performance

The primary performance measure of a solar cell is efficiency $\eta$, a measure of the percentage of energy from solar radiation $P_{in}$ that can be converted into electrical energy by the cell $P_{MPP}$. Efficiency is calculated from the maximum-power point (MPP, explained in detail in Part E), where the product of the cells operating current and voltage is the greatest. Efficiency is governed by the chemical composition of the cell and environmental conditions. It can even vary slightly between cells of the same type because of defects to the crystalline structure at a molecular level caused by either radiation damage or age.

One important characteristic of a PV cell is that the output voltage remains nearly constant regardless of the cell size. Furthermore, the efficiency of a cell and the output voltage remain relatively constant as the intensity of light changes. An increase in input power (from the sun) has a linear relationship with the output power of the cell as the output current increases. This relationship is illustrated for a generic PV cell in Figure 3.

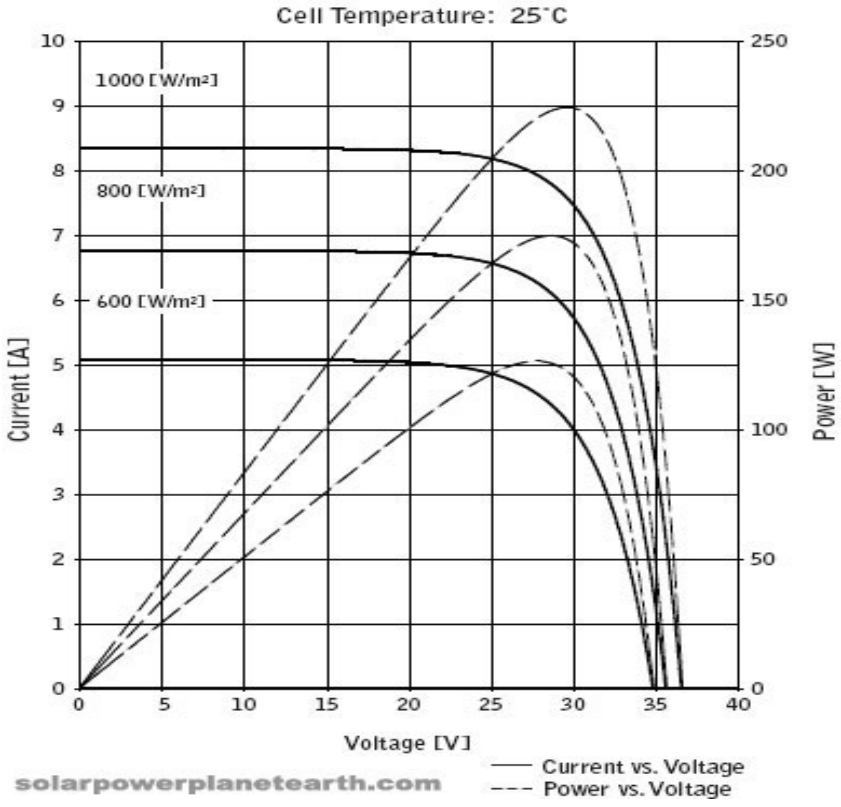


Figure 3. Relationship between input power and I-V curve. Source [18].

The efficiency can change, however, with changes in the surrounding environment. Specifically, changes in cell temperature causes quantifiable variations in performance. An individual solar cell with an open circuit voltage $V_{OC}$ of 0.7 V will see a reduction in output by approximately 2.0 mV/°C [16]. This effect is most pronounced in PV cells due to the internal heating that occurs from photons of sunlight interacting with the semiconductor material and occurs in any climate. This heating can be partially dissipated depending on the outside ambient temperature and airflow-induced cooling. Consequently, operating in cooler climates and at higher altitudes (where temperatures are lower assuming a standard adiabatic lapse rate) results in slightly higher PV performance.

A string of PV cells is also significantly affected by shading or other impairment to even a single cell. This is because the total current through any series-connected string of cells, like any other electric circuit, can only be as high as the current through any single cell. Excess current unable to pass through a shaded or damaged cell is lost as heat in the remaining cells, potentially causing additional damage. This negative shading effect can be mitigated by adding a diode to each string of cells. This diode protects against reverse current losses in a larger system but decreases the output voltage of the string by approximately 0.7 V when operating normally.

## C. SOLAR INSOLATION

The amount of solar energy available to a solar cell is dependent on a number of elements, principally the location on the earth, time of year, and the time of day. These three factors, and to a lesser extent the elevation and local climate, determines the maximum amount of solar energy that reaches the surface of the earth and lower atmosphere where SUAS operate. Fortunately, models exist that predict the solar irradiance, or insolation, the amount of solar energy that reaches a unit area on the earth.

### 1. Air Mass Levels

Solar radiation from the sun is relatively constant and spreads at a known rate. At the earth's average distance from the sun, this solar constant $I_{SC}$ has an accepted power density of 1367 W/m$^2$ [19], approximately 95% of which is concentrated over a spectrum from 0.2 to 2.0 μm. Based on the time of day and latitude, between 30% and 90% of this

energy is absorbed, reflected, or scattered by ozone, dust, air molecules, and water vapor before reaching the surface [20]. When the sun's elevation is low over the horizon relative to a viewer on the surface of the earth, the solar radiation passes through even more atmosphere before reaching the earth's surface. An illustration of this effect illustrated in Figure 4 depicts the basic components of the measurement of air mass, "the ratio of the distance that solar radiation travels through the earth's atmosphere, to the distance it would travel if the sun were directly overhead" [20].

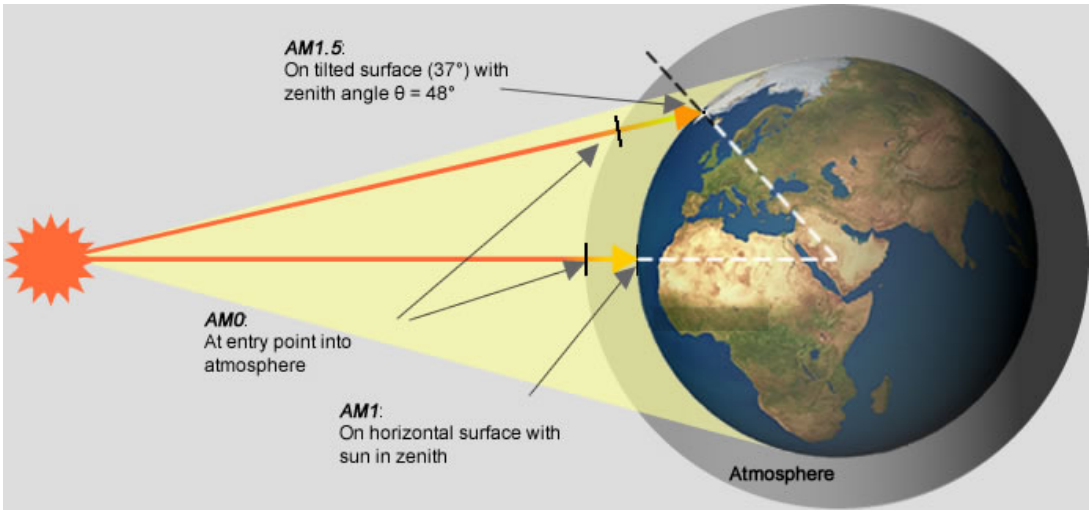


Figure 4. Illustration of air mass. Source [21].

By convention, radiation in space just outside the earth's atmosphere is said to have an air mass of zero (AM0). Solar radiation reaching the surface of the earth from directly overhead, a zenith angle of 0°, passes through an air mass of 1.0 (AM1). At a zenith angle of 60°, solar radiation passes through twice as much atmosphere as when the sun is directly overhead for an air mass of 2.0. Most research modeling typical conditions in North American latitudes uses the approximation of an air mass of 1.5 (AM1.5), which equates to a power density of 1000 W/m$^2$.

## 2. Calculating Air Mass and Irradiance

With an accurate calculation of the irradiance reaching the atmosphere, we next calculate the air mass and solar insolation reaching the surface, or for our purposes, an

aircraft flying at low altitude. Air mass varies across the Earth with changes in latitude; sunlight passes through more atmosphere to reach the North and South Poles than areas near the equator. The sun's arc across the sky also changes seasonally, and the specific elevation of the sun along a given arc changes constantly throughout a day. Three primary factors, latitude, day of year, and time of day, must be considered to accurately calculate air mass. Additionally, for our application, incorporating a measurement of the height above ground of an aircraft has an effect of secondary importance but is easily incorporated in most existing models.

Various algorithms have been developed to approximate air mass and solar insolation which provide varying degrees of complexity and accuracy. In this research, we adopt the analytical model used in [22] by the Naval Research Lab because it is capable of deriving all required quantities from basic latitude and day of year information and can dynamically incorporate desired aircraft altitude and attitude attributes.

### *a. Fine-Tuning the Solar Constant*

Accurately calculating the solar irradiance at any point in the atmosphere first depends on an accurate calculation of the irradiance reaching the Earth. The elliptical orbit of the earth around the sun causes a slight variance in the intensity of solar radiation just outside the earth's atmosphere, as much as ±3.4% from the annual average [20]. A maximum occurs around January 4 and a minimum around July 5. This variation can be approximated by fine-tuning the solar constant $I_{SC}$

$$I_o = I_{sc}\left[1 + 0.034\cos\left(\frac{360N}{365.25}\right)\right] \quad \left(\mathrm{W/m^2}\right) \tag{1}$$

where $I_o$ is solar irradiance just outside the earth's atmosphere and $N$ is the day of the year starting on January 1 [20].

### *b. Calculating Solar Azimuth and Elevation*

The solar zenith angle $z$, elevation angle $e$, and azimuth angle $a$ can be calculated from a knowledge of the aircraft latitude $lat$, year fraction $\gamma$, declination angle $\delta$, and hour angle $\omega$ using [12]:

$$z = \cos^{-1}\left(\cos(lat)\cos(\gamma)\cos(\omega) + \sin(lat)\sin(\delta)\right), \tag{2}$$

$$e = 90^{\circ} - z \ , \tag{3}$$

$$\text{and } a = \left(\frac{\omega}{|\omega|}\right)\frac{\left|\cos^{-1}\left(\cos(z)\sin(lat) - \sin(\delta)\right)\right|}{\sin(z)\cos(lat)} + \pi \, , \tag{4}$$

where the year fraction in radians is determined from

$$\gamma = (N-1)\left(\frac{360}{365}\right)\left(\frac{\pi}{180}\right), \tag{5}$$

the declination angle is given by

$$\begin{aligned}\delta = {} & 0.006918 - 0.399912\cos(\gamma) + 0.070257\sin(\gamma) - 0.006758\cos(2\gamma) \\ & + 0.000907\sin(2\gamma) - 0.002697\cos(3\gamma) + 0.00148\sin(3\gamma)\end{aligned} \, , \tag{6}$$

and the hour angle in radians is given by

$$\omega = (t_{solar} - 12)\left(15\,{}^{\deg}\!/_{\mathrm{hr}}\right)\left(\frac{\pi}{180}\right). \tag{7}$$

The solar time $t_{solar}$ used in [12] is based on a calculation of

$$t_{solar} = t_{utc} + 4lon/60 + EoT/60 \, , \tag{8}$$

which is a variation of coordinated universal time (UTC) $t_{utc}$ modified to account for the longitude *lon* in degrees east (+) or west (-) and an empirical adjustment to account for the eccentricity of the earth's orbit called the equation of time *EoT* [12] given in minutes from

$$EoT = 0.2292\left(0.075 + 1.87\cos(\gamma) - 32.08\sin(\gamma) - 14.62\cos(2\gamma) - 40.09\sin(2\gamma)\right). \tag{9}$$

### *c. Weather and Environmental Effects*

After calculating of the solar zenith angle, the direct atmospheric transmittance $\tau_{driect}$ can be computed. The air mass model can be further refined to account for the effects of a local climate model [23] based on

$$\tau_{direct} = r_0 a_0^* + r_1 a_1^* e^{\left(-r_k k^*/\cos(z)\right)} \tag{10}$$

where the constants $a_0$, $a_1$, and $k$ are based on a flight altitude $h$ in km above mean sea level. The parameters $a_0^*$ , $a_1^*$ , and $k^*$ are computed, respectively, from

$$a_0^* = 0.4237 - 0.00821(6-h)^2 \, , \tag{11}$$

$$a_1^* = 0.5055 + 0.00595(6.5-h)^2 \, , \tag{12}$$

$$\text{and } k^* = 0.2711 + 0.01858\left(2.5 - h\right)^2 . \quad (13)$$

The constants $r_0$, $r_1$, and $r_k$ are corrections for the specific climate type in accordance with Table 2.

Table 2. Climate correction for atmospheric transmittance model. Adapted from [23].

| Climate Type | $r_0$ | $r_1$ | $r_k$ |
|---|---|---|---|
| Tropical | 0.95 | 0.98 | 1.02 |
| Midlatitude summer | 0.97 | 0.99 | 1.02 |
| Subarctic summer | 0.99 | 0.99 | 1.01 |
| Midlatitude winter | 1.03 | 1.01 | 1.00 |

### *d. Indirect or Diffuse Irradiance*

A portion of the solar radiation scattered by the atmosphere still finds its way to the surface of the earth, appearing to arrive from directions different from the direct irradiance. This so-called diffuse or indirect irradiance, which, for example, allows us to see in an area shaded from direct sunlight, accounts for 10–20% of total irradiance on a clear day and nearly 100% of total irradiance on an overcast day [20]. Diffuse transmittance $\tau_{diffuse}$ is determined empirically from [24]

$$\tau_{diffuse} = 0.271 - 0.294\tau_{direct} \quad (14)$$

based on the direct transmittance.

### *e. Calculating Solar Insolation and Power*

Finally, after determining the direct and diffuse transmittance, total clear sky direct normal radiation $I_{direct}$ can be determined from the solar irradiance according to

$$I_{direct} = I_o \tau_{direct} \ , \quad (15)$$

and the diffuse insolation $I_{diffuse}$ from

$$I_{diffuse} = I_o \tau_{diffuse} \ . \quad (16)$$

The total direct and indirect normal solar insolation $I$ is then determined from

$$I = I_{direct} + I_{diffuse} . \quad (17)$$

The total power available from a solar PV system $P_{solar}$, which accounts for the size and angular difference between the PV array and the sun, can now be calculated from

$$P_{solar} = \left( I_{direct} \cos(i) + I_{diffuse} \right) S_c \eta_{total} \tag{18}$$

where $i$ is the incidence angle between the PV panel and the sun as determined in the next section. The surface area of the solar array $S_c$ is determined by the aircraft configuration, and the total efficiency $\eta_{total}$ is a combination of the efficiencies of the solar array, the maximum-power point tracking (MPPT), and the DC-DC converter.

## D. SOLAR INCIDENCE ON A WING

Maximum solar energy is delivered to a PV panel only when that panel (the surface normal) is directly facing the sun. At any other incidence angle, the solar energy is reduced by a factor of cos($i$) where $i$ is the incidence angle between the PV panel and the sun. This relationship is depicted graphically in Figure 5, where the incidence angle is represented by the symbol $\theta_z$.

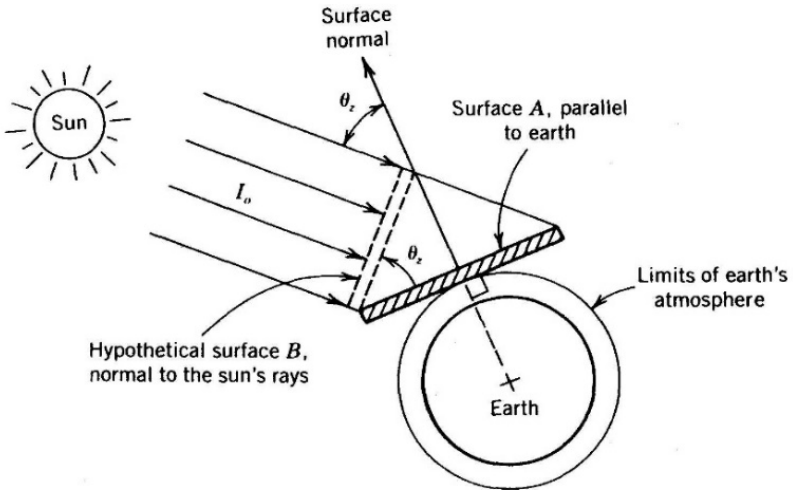


Figure 5. Solar irradiance on a surface parallel to the ground. Source [20].

This calculation may be relatively straightforward in the case of a terrestrial panel mounted in a fixed position on the ground or a building; however, it is complicated significantly when the panel is mounted to the wing or fuselage of an aircraft that can dynamically change its pitch, bank, and yaw.

Every axis of an aircraft's attitude affects the incidence angle toward the sun as well as affecting the magnitude of the effect from every other axis. These various factors and their interactions with the incidence angle are calculated from [12]

$$\begin{aligned}\cos(i) &= \cos(-e)\cos(az)\sin(\psi)\sin(\phi) - \cos(-e)\sin(az)\cos(\psi)\sin(\phi) \\ &+ \cos(-e)\cos(az)\cos(\psi)\sin(\theta)\cos(\phi) + \cos(-e)\sin(az)\sin(\psi)\cos(\theta)\cos(\phi) \\ &- \sin(-e)\cos(\theta)\cos(\phi)\end{aligned} \quad (19)$$

where $\psi$ is the aircraft yaw angle, $\phi$ is the bank angle (positive to the right), $\theta$ is the pitch angle, and *az* is the "azimuth" angle measured from the aircraft tail to the direction of the sun in a clockwise direction.

In the case of the Puma, the outer wing segments have a 10° dihedral. The incidence angle is, therefore, different and must be calculated separately for each of the three upper wing surfaces. For the outer wing surfaces, 10° must be added or subtracted from the roll angle such that $\phi_{array} = \phi \pm 10°$ replaces $\phi$ in (19).

On the Puma specifically, fuselage shading of the PV cells is generally not an issue because the wing is mounted above the fuselage. Shading may occur in some instances when the aircraft bank angle is close to or exceeds the sun's elevation angle from the horizon.

## E. MAXIMUM POWER POINT TRACKING

Maximum electrical power transfers from a source to a load when the impedance of the source and load match. In our application, unfortunately, the load is variable depending on aircraft flight parameters, and the source is variable with changing solar irradiance over the course of a day or during maneuvers. To provide the greatest possible benefit, our system should be designed to provide the greatest possible power output from the limited number of solar cells in any environment, not just under optimum conditions. This is accomplished through decoupling the load from the source and inserting additional circuitry to track the MPP of the solar panel, adjusting the output voltage to provide maximum power in any given configuration.

An example of the changing MPP is shown in Figure 6. In this example on a generic solar array, as irradiance changes from 1000 W/m$^2$ to 600 W/m$^2$, the MPP decreases from

30.0 V to 27.5 V. A number of techniques and algorithms have been developed to conduct MPPT and are implemented in a variety of commercial power electronics with efficiencies $\eta_{MPPT}$ as high as 99% [25]. The optimized power output from the system utilizing an MPPT easily exceeds the insertion losses from the additional hardware.

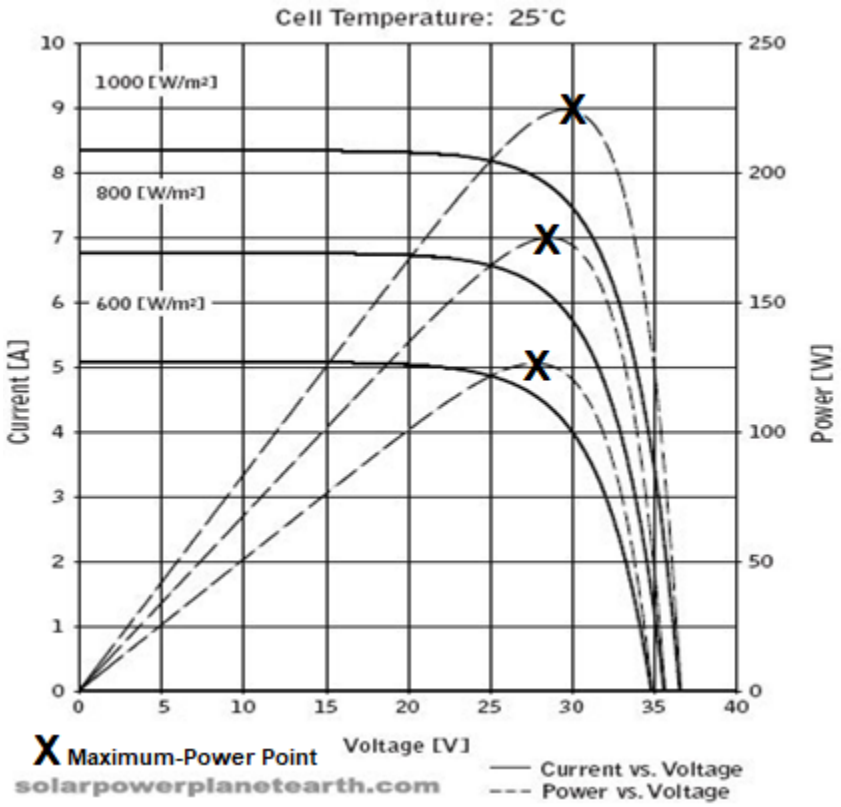


Figure 6. Changing MPP with changing input irradiance. Adapted from [18].

The proposed solar panels on the RQ-20 Puma are subdivided into three separate arrays because of the outer panel wing dihedral. As depicted in Figure 7, the 10° wing dihedral of the outer wing sections causes the solar incidence angle to differ between the three wing sections and corresponding solar panels for all phases of flight.

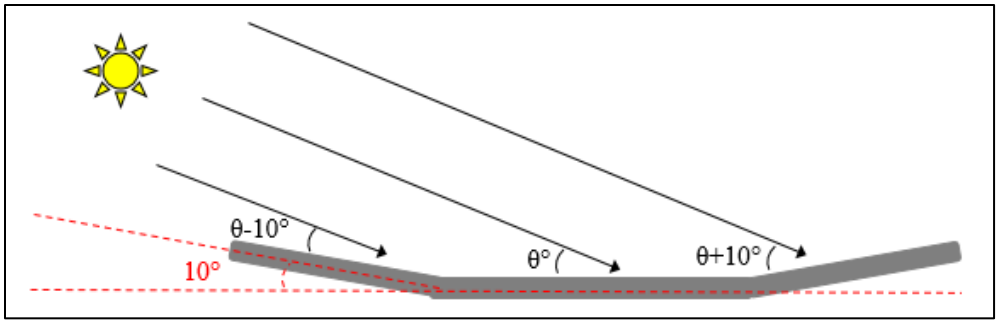


Figure 7. RQ-20 Puma wing with 10° outer panel wing dihedral

This difference can be as much as 20° between the two outer panels when the aircraft track is perpendicular to the solar azimuth. This results in the outer panels and the center panel usually having different maximum-power points. Previous research specifically examining different MPPT configurations for the Puma concluded that the optimum distribution of MPPTs for maximum power generation on the Puma wing is to have a separate MPPT for each of the three wing sections [25].

## F. BATTERY CHARGING

In this section, we review several aspects of the interface between the PV array and the battery used to power the aircraft. After maximizing the power output with a MPPT, the electrical energy must be managed to most efficiently operate aircraft systems, charge, or discharge the battery.

### 1. DC-DC Converters

Battery charging requires an input voltage higher than the battery voltage. A PV charging system can theoretically be designed such that the output voltage of the string of cells is always above the battery voltage. When environmental conditions are variable, however, the maximum power from a PV array is at an ever-changing voltage level. Furthermore, the PV array on the wing of a SUAS may not be optimally sized to provide this required voltage under even peak conditions. For these reasons, the incorporation of a relatively small, lightweight, and inexpensive DC-to-DC converter ensures that the optimized power delivered from a PV array, regardless of its voltage, is sufficient to support the aircraft's power requirements or to charge the battery.

### 2. Load Balancing

The battery that powers the Puma is composed of six sets (electrically connected in parallel) of six series-connected individual Li-Ion cells. Each of the six cells provides 3.0 to 4.2 V that combined provide the 25.2V battery rating. To prevent over charging or over discharging of individual cells, Li-Ion batteries of this size must have load-balancing circuitry that monitors the load and charging of cells individually. Damage, fire, or explosion can result from a failure to properly balance the charging process [6].

### 3. Efficiency

A battery stores energy in a chemical form. When discharged, the battery converts stored chemical energy back into electrical energy. The battery efficiency $\eta_{\text{batt}}$ accounts for the conversion process from electrical to chemical, or back, and is around 90% each way [6]. Electrical energy from a PV array that is able to directly power system components is not subject to this loss because the energy stays in electrical form. The electrical-to-mechanical losses (an additional 10–35% of the electrical energy after leaving the battery) produced in powering the UAV motor are accounted for in subsequent chapters where we measure current input to the motor to simultaneously account for motor power required and losses concurrently.

An optimum integration of a PV array on the SUAS, therefore, connects the array in parallel with the battery in such a way as to be able to power the load directly, supplemented by the battery only as necessary. This eliminates efficiency losses from converting energy into the battery and back out again. In this configuration, if excess power is available to fully power the load, the PV array can also charge the battery with an overall efficiency of approximately 81% from combining the charging and discharging efficiency:

$$\eta_{charge}\eta_{discharge} = 2\eta_{batt} = 2(0.9) = 0.81. \tag{20}$$

### 4. Battery Limits

A battery cannot be charged above its maximum state. If a PV array is capable of charging a battery in flight, once the battery reaches its maximum charge, additional energy provided by a PV array is lost.

## 5. Lithium-Ion Battery Capacities

The state of charge of a Li-Ion battery can be closely approximated by measuring the battery voltage. This can be a useful relationship to monitor the rate of charge or discharge of an aircraft battery under different flight profiles or when being augmented by a PV array. As illustrated in Figure 8, a fully charged battery initially discharges at an exponential rate for a relatively short period. Then, the majority of the battery's stored energy is discharged through the "nominal region" at a roughly linear rate. The final approximately 10% of the battery's usable charge again discharges at an exponential rate with a very steep drop off until reaching the discharge cut-off voltage. Because most of the change occurs in a linear region, we can interpolate within a given top and nominal voltage range of the battery to accurately predict the state-of-charge and remaining capacity based on a measured voltage within that range.

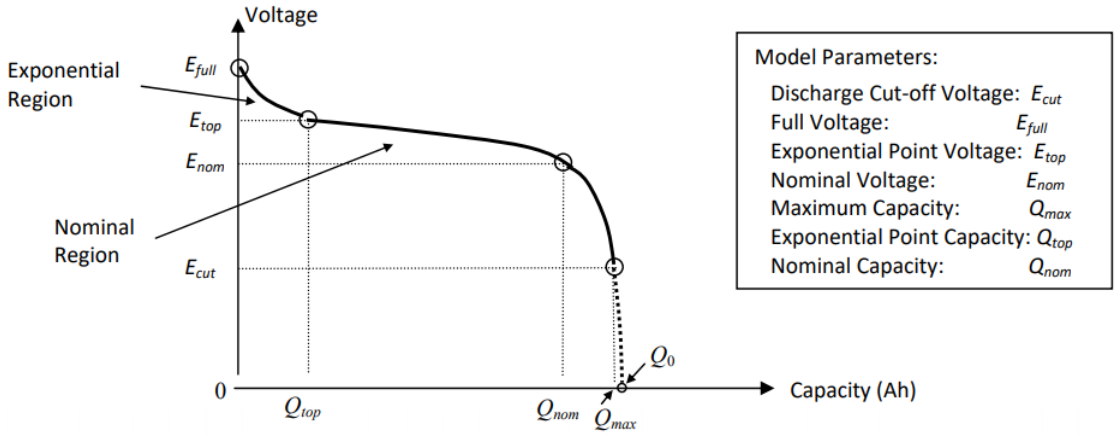


Figure 8. Typical battery discharge curve. Source [26].

A measurement of the energy stored in a battery $W_{batt}$ is made by multiplying the average voltage during discharge $E_{av}$ with the stored charge of the battery $Q_{rated}$. Because of the linear discharge relationship, we assume the average voltage is related to a given maximum voltage $E_{full}$ and nominal voltage $E_{nom}$ by [27]

$$W_{batt} = E_{av} Q_{rated} = \frac{E_{full} + E_{nom}}{2} Q_{rated} . \tag{21}$$

The Puma's Li-Ion polymer battery is rated by the manufacturer to have a fully charged voltage of 25.2 V and a capacity of 13.5 Amp-hrs [15]. The battery is considered to be low at 18.8 V when approximately 10 to 15 minutes of flight time remains (5 to 10% of total flight time); an emergency low condition exists when a voltage of 17.4 V is reached, and the aircraft must land immediately [15]. Although complete and detailed battery characteristics are not provided, if we assume from the given information an $E_{full}$ of 25.2 V and $E_{nom}$ of 18.8 V, we can apply (17) to determine the total energy capacity of the puma battery in this range as

$$W_{batt} = \frac{25.2\text{V} + 18.8\text{V}}{2} 13.5\text{Ah} = 297 \text{ Wh} . \tag{22}$$

Within this voltage range of 25.2 to 18.8 V, the Puma battery should discharge in a generally linear fashion from 100% down to 10% of the rated capacity. We can approximate a general relationship between the state-of-charge and voltage range as

$$\frac{SOC}{E_{range}} = \frac{100\% - 10\%}{25.2\text{V} - 18.8\text{V}} = \frac{90\%}{6.4\text{V}} = 14.1 \%/\text{V} . \tag{23}$$

A similar relationship between energy capacity of the battery and voltage range is

$$\frac{W_{batt}}{E_{range}} = \frac{0.9 * 297\text{Wh}}{6.4\text{V}} = 41.77 \text{ Wh}/\text{V} . \tag{24}$$

This relationship means that for every 1.0 V decrease in the measured battery voltage, the state of charge decreased by 14.1% and 41.77 Wh are consumed.

Without an ability to directly measure these battery characteristics under realistic conditions, it is important to note that the slope of the discharge curve varies significantly under different loads [26]. Slight variations are also common between batteries of the same type and will change for an individual battery with age and the depth of previous charge and discharge cycles.

THIS PAGE INTENTIONALLY LEFT BLANK

# III. TESTING AND ANALYSIS

In this chapter, we begin with a summary of aircraft and electronics performance data that was gathered during laboratory bench tests and from a series of actual flights. Our selected PV array solution is summarized and then simulated across a variety of realistic environments. Next, we assess the performance of the additional power electronics chosen. Finally, we summarize the effects of the additional weight and cost of all components of this PV system.

## A. AIRCRAFT DATA

To make accurate predictions of aircraft flight endurance and performance with PV augmentation, accurate measurements of power consumption through various flight profiles and throttle settings are necessary. Testing previously done with the Raven SUAS [4], [7] used a very effective method of simultaneously measuring voltage and current demand at the battery terminals to generate a very accurate picture of all power requirements. Unfortunately, the "smart battery" of the Puma is configured in such a way that that a similar technique of testing individual battery leads between the battery and aircraft it is not possible.

As a workaround, a two-part method was developed to collect the required data. This method utilized a fully configured aircraft on a test bench in a laboratory environment (where external factors could be isolated and controlled) where possible. For subcomponents that could not be isolated or individually measured, approximations for the Puma are based on subcomponent measurements from the RQ-11 Raven, a similar SUAS from the same manufacturer with similar operating characteristics.

### 1. Test Bench Data Collection on RQ-20 Puma

Testing on the RQ-20 system was completed at the Evolving Resources Inc. (ERI) facility in Camarillo, CA in March 2018 using two different aircraft configurations. First, the aircraft was assembled on a test stand without the wing, which contains no electrical components. This layout was used to test power output from the avionics assembly to the

flight control servos and strobe lights located in the tail of the aircraft and power output to the EO/IR payload located between the battery and the avionics bay. Voltage measurements were directly read from the VO hand controller; current measurements were obtained with a Klein Tools CL800 Digital Clamp Meter on wires connecting the subcomponents to the avionics assembly. Next, the test stand shown in Figure 9 was utilized to isolate the battery, avionics assembly, and motor outside of a physical aircraft fuselage for ease of measuring only the motor performance.

Figure 9. Motor test stand at ERI with digital clamp meter attached

Voltage and current measurements were obtained in the same manner as with the first test bench setup. A summary of the major subassemblies and the test setups utilized are depicted in Figure 10.

On the aircraft test stand, measurements were made both before and after subassembly tests in a neutral state with the payload stowed, no flight control movement, and all strobe lights off. Next, individual components were deployed and/or activated while changes in current were observed and recorded. Each test was repeated several times to ensure accuracy of the results, which are summarized in Table 3. The Current Difference

is the additional current demand on the system for the specified condition relative to the baseline current requirement for that section of the aircraft. The calculated power indicates the power requirement from a neutral state or the additional power requirement of activating an individual subcomponent. Both the flight control servos and payload recorded some current draw even when the subcomponents were not in their active states. Both subcomponents indicated increased power demand when the systems were in use with a nearly immediate return to the neutral state when the component ceased being used. There was no perceptible difference with visible or IR strobe lights in use or with the IR illuminator on or off.

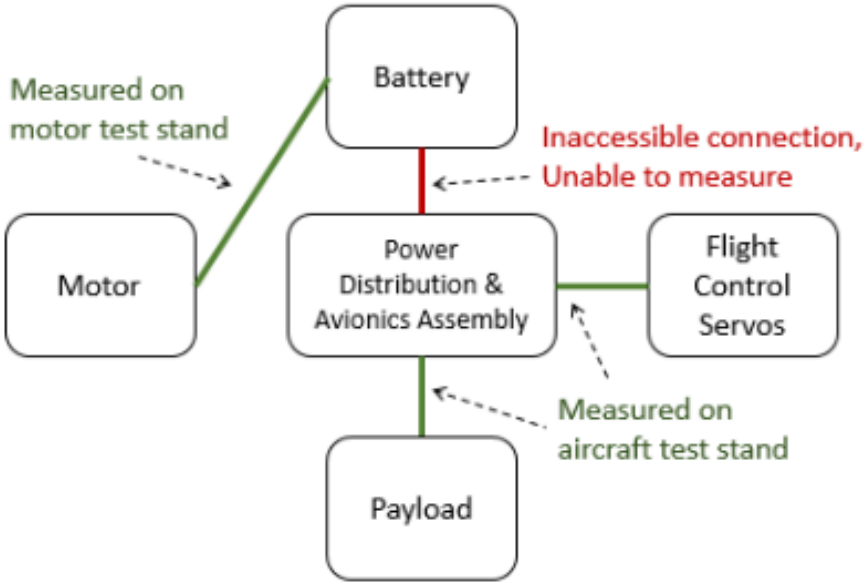


Figure 10. Block diagram of Puma subassemblies for power measurements

On the aircraft motor test stand, a series of measurements were taken over four test runs. The first two test runs were from a moderately charged 65% battery (initially indicating 22.9 V) during a rising throttle sequence and then a falling throttle sequence. After an initial measurement with the throttle set at 0%, the throttle was advanced first to 10% and then in 5% increments (the smallest increment manually selectable by the user) until the throttle reached 100%. At each increment, voltage and current supplied to the motor were recorded after 2 to 3 seconds when the current stabilized. From 100%, the

throttle was then decreased in 5% increments until again reaching 0%. Test runs three and four were conducted in an identical fashion from a 40% charged battery (21.9 V starting voltage). Data for all four test runs is recorded in Table 4.

Table 3. Measurements from Puma test stand

| Wire to tail section | Voltage (V) | Current (A) | | Power (W) |
|---|---|---|---|---|
| | | Measured | Difference | |
| Flight controls neutral (baseline) | 22.5 | 0.16 | - | 3.6 |
| Flight control servos active | 22.5 | 0.23 | 0.07 | 1.6 |
| Strobe lights / Illuminator | 22.5 | 0.16 | < 0.005 | <0.1 |
| Wire to payload section | | | | |
| Payload stowed (baseline) | 22.3 | 0.27 | - | 6.0 |
| Payload deploying (2-3 sec.) | 22.3 | 0.45 (peak) | 0.18 | 4.0 |
| Payload deployed, stationary | 22.3 | 0.31 | 0.04 | 0.9 |
| Payload deployed, moving | 22.3 | 0.34 | 0.07 | 1.6 |
| Payload stowing (2-3 sec.) | 22.3 | 0.38 (peak) | 0.11 | 2.5 |

The motor used on the test stand was a new motor. ERI technicians performing functional checks on motors in the course of depot-level maintenance and repair note a roughly 10% decrease in motor efficiency between new and old motors [28].

The data in Table 4 indicates a dramatic increase in current demand as the throttle increasd above 50%. Power is clearly not related to throttle percent in a linear fashion. There is also a notable voltage drop beginning around the same point that the power/throttle shows significant increases. From the third and fourth test runs there also appears to be a built in low-voltage protection for the system that does not let the battery voltage decrease past a certain point. In runs 3 and 4, after the battery voltage decreased to 17.5 V at 95% throttle, an increase in throttle did not create any additional power demand. Though smaller, a similar effect was present during the first and second runs with the stronger battery. The increase in power from 95% to 100% throttle is less than the increase from 90% to 95% throttle.

Table 4. Measurements from motor test stand

| Throttle | Run 1 | | Run 2 | | Run 3 | | Run 4 | |
|---|---|---|---|---|---|---|---|---|
| | V [a] | I [b] | V | I | V | I | V | I |
| 0 % | 22.9 | 0.08 | 22.5 | 0.18 | 21.9 | 0.13 | 21.5 | 0.36 |
| 10% | 22.9 | 0.11 | 22.5 | 0.34 | 21.9 | 0.21 | 21.5 | 0.50 |
| 15% | 22.9 | 0.16 | 22.5 | 0.39 | 21.9 | 0.26 | 21.5 | 0.55 |
| 20% | 22.9 | 0.24 | 22.5 | 0.49 | 21.9 | 0.34 | 21.4 | 0.65 |
| 25% | 22.9 | 0.40 | 22.5 | 0.65 | 21.9 | 0.52 | 21.4 | 0.82 |
| 30% | 22.8 | 0.67 | 22.4 | 0.93 | 21.8 | 0.80 | 21.3 | 1.11 |
| 35% | 22.8 | 1.04 | 22.5 | 1.32 | 21.8 | 1.19 | 21.3 | 1.51 |
| 40% | 22.6 | 1.58 | 22.5 | 1.85 | 21.8 | 1.75 | 21.2 | 2.08 |
| 45% | 22.6 | 2.30 | 22.1 | 2.58 | 21.6 | 2.52 | 21.2 | 2.88 |
| 50% | 22.6 | 3.24 | 22.1 | 3.53 | 21.6 | 3.53 | 21.0 | 3.88 |
| 55% | 22.6 | 4.47 | 22.9 | 4.78 | 21.4 | 4.81 | 20.9 | 5.21 |
| 60% | 22.3 | 6.02 | 21.8 | 6.37 | 21.2 | 6.40 | 20.7 | 6.91 |
| 65% | 22.1 | 7.91 | 20.5 | 8.42 | 21.0 | 8.45 | 20.5 | 9.07 |
| 70% | 21.9 | 10.28 | 20.3 | 11.02 | 20.7 | 10.97 | 20.2 | 11.81 |
| 75% | 21.5 | 13.18 | 20.9 | 14.20 | 20.1 | 14.05 | 19.8 | 15.17 |
| 80% | 21.2 | 16.74 | 20.4 | 18.30 | 19.9 | 17.92 | 19.3 | 19.48 |
| 85% | 20.7 | 21.28 | 19.8 | 23.51 | 19.4 | 22.87 | 18.4 | 25.34 |
| 90% | 19.7 | 31.29 | 18.7 | 34.37 | 18.3 | 33.80 | 17.2 | 36.96 |
| 95% | 18.9 | 38.24 | 18.7 | 38.32 | 17.5 | 38.56 | 17.5 | 38.56 |
| 100% | 18.7 | 38.28 | 18.7 | 38.28 | 17.5 | 38.56 | 17.5 | 38.56 |

[a]V: Measured voltage, units of volts.

[b]I: Measured current, units of amps.

After plotting the aggregated data as power in Figure 11, we observe that the power demand on all four runs is nearly identical. This suggests that for a given throttle selection, the motor demands a consistent amount of electrical power (up to the voltage limit of the battery) regardless of the charge state of the battery. The average power for each throttle setting is summarized in Table 5.

Table 5. Summary of power requirements for throttle setting

| Throttle | Power (W) | Throttle | Power (W) | Throttle | Power (W) | Throttle | Power (W) |
|---|---|---|---|---|---|---|---|
| 0% | 4.1 | 30% | 19.3 | 55% | 104.4 | 80% | 365.2 |
| 10% | 6.4 | 35% | 27.9 | 60% | 138.0 | 85% | 454.0 |
| 15% | 7.5 | 40% | 39.8 | 65% | 177.7 | 90% | 628.3 |
| 20% | 9.5 | 45% | 56.0 | 70% | 228.6 | 95% | 696.7 |
| 25% | 13.2 | 50% | 77.2 | 75% | 290.7 | 100% | 695.5 |

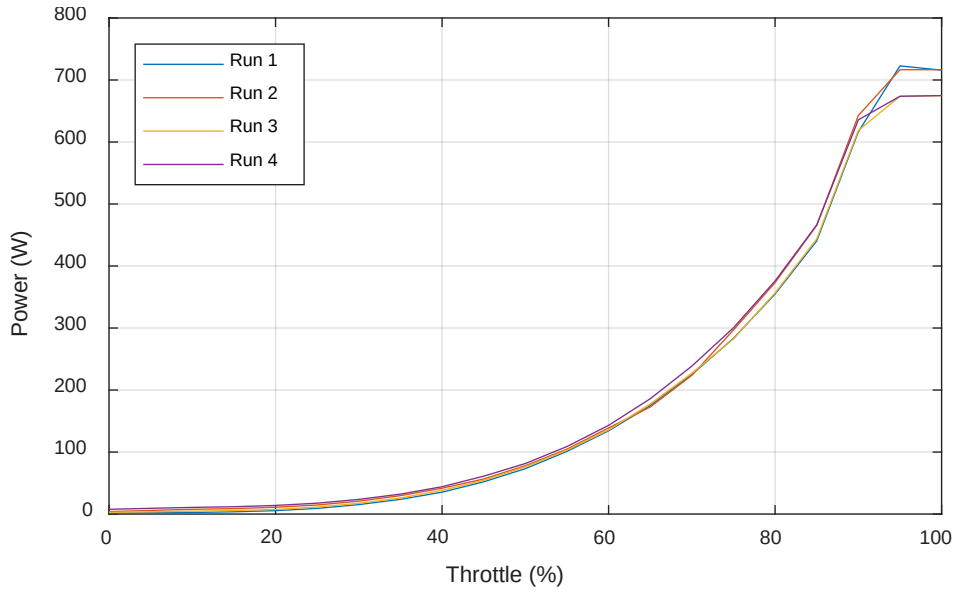


Figure 11. Power required and throttle setting from test bench runs 1 through 4

To allow for more precise interpretation and calculations required in other sections of this research, we desired an equation that could represent the power-throttle curve. We used MATLAB curve fitting tools to model the average power required as a function of throttle setting. We excluded the data above 90% throttle because in our observations we appear to have reached a power limiting threshold above 90%. Some of the goodness-of-fit statistics from the two polynomial and two exponential curve fits that were tested are shown in Table 6.

Table 6. Goodness of fit statistics of power throttle curve fit techniques

| Curve Fit | SSE | $R^2$ | Adj $R^2$ |
|---|---|---|---|
| Quadratic Polynomial | 16765 | 0.971 | 0.967 |
| Cubic Polynomial | 2886 | 0.995 | 0.994 |
| Single-Term Exponential | 1273 | 0.998 | 0.998 |
| Double-Term Exponential | 1209 | 0.998 | 0.997 |

The single-term exponential curve fit was chosen because it provides a very close fit to the data as indicated by the $R^2$ value very close to 1.0 and having among the lowest

SSE of all other models evaluated. The single-term exponential model is also a relatively straightforward expression of the form

$$f(x) = ae^{bx}. \tag{25}$$

We used MATLAB to calculate coefficients (with 95% confidence bounds) of $a$ = 5.82 ± 0.96 and $b$ = 0.052 ± 0.002. These coefficients provide the following approximation of the power-throttle relationship, allowing us the ability to calculate motor power:

$$P_{motor} = 5.82e^{0.052Throttle}. \tag{26}$$

To visualize how closely the predicted model fits the data, we plotted the single-term exponential curve fit from (26) against the average throttle requirements summarized in Table 5. The results shown in Figure 12 indicate a very close fit to the data across the modeled range of 0–90%. Flight test data gathered in future sections shows that the aircraft throttle is set to 90% or less for over 99.5% of recorded flight time, even during all aircraft climbs. We, therefore, believe this model will be satisfactory in representing aircraft performance across all relevant profiles.

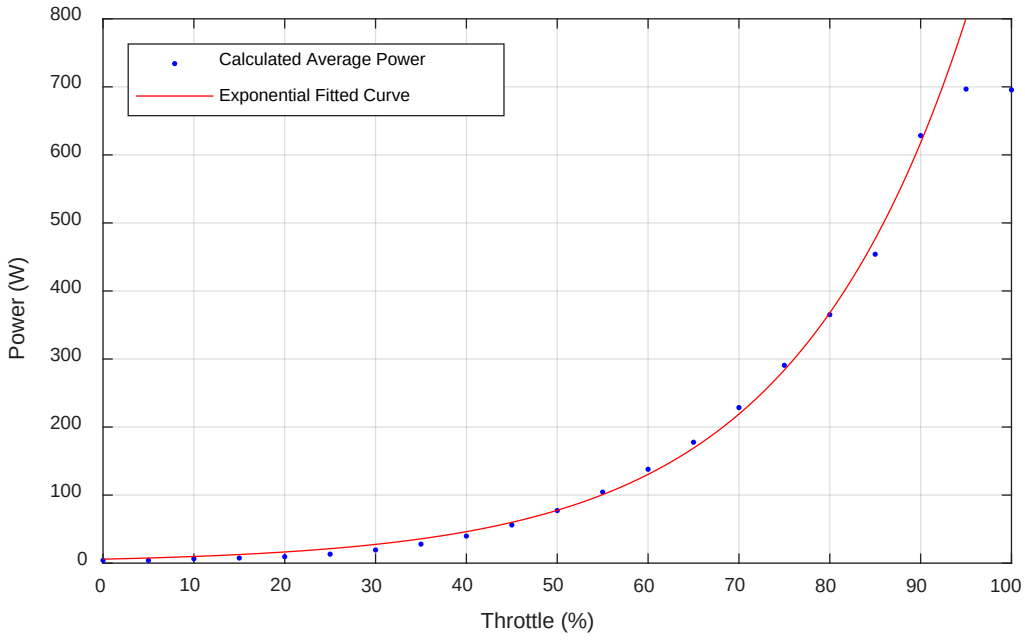


Figure 12. Plot of motor power curve fit against calculated average power

## 2. Supplemental Data from RQ-11 Raven

One of the limitations of the testing equipment available and the electronics configuration of the Puma is that a direct measurement of total current between the battery and the avionics assembly is not possible without destructive disassembly of the airframe. The avionics assembly contains the GPS receiver, pitot-static sensors, flight control processors, radio transmitter and receiver, and serves as a power distribution hub for the servo/strobe light assembly and the payload. Power to the servo assembly and payload were directly measured as described in the previous section, but power required for the remaining avionics subsystems could not be directly measured.

Fortunately, an approximation of the avionics and transmitter power requirements for the Puma can be based on the power requirements for very similar systems installed on the RQ-11 Raven, which can be easily measured. The two aircraft are similar in that they are in current production by the same manufacturer, fly with an identical control configuration, interface with the same ground control station, and perform an identical mission.

To isolate the power required by the RQ-11 avionics and transmitter subcomponents, a laboratory test bench setup was utilized where voltage and current demands were simultaneously measured in real-time as individual components were activated or disabled. Measurements were taken with a Fluke 45 dual-display multimeter in a Naval Postgraduate School laboratory. The results of these measurements are recorded in Table 7 and closely mirror measurements taken by other research in 2014 [9].

Table 7. Measurements from Raven test stand

| Tested Assembly Configuration | Voltage (V) | Current (A) | | Power (W) |
|---|---|---|---|---|
| | | Measured | Difference | |
| Tail and payload removed | 24.8 | 0.36 | - | 8.9 |
| Tail installed, payload removed | 24.8 | 0.44 | 0.08 | 2.0 |
| Tail removed, payload installed | 24.8 | 0.61 | 0.25 | 6.2 |
| Full aircraft, controls neutral | 24.8 | 0.64 | 0.28 | 6.9 |
| Flight control servos active | 24.8 | 0.71 | 0.07 | 1.7 |
| Strobe lights on | 24.8 | 0.65 | 0.01 | 0.2 |
| Payload installed, video on | 24.8 | 0.71 | 0.07 | 1.7 |

The first measurement in Table 7 is the closest possible measurement of the power requirement for the avionics/transmitter assembly alone; in the case of the Raven, the value also includes current to the motor (0% throttle in this test). The assumption that the two aircraft platforms operate with similar power requirements can be validated by comparing what is known about the individual components that can be measured independently. The comparison in Table 8 indicates that power requirements are generally very similar between the two systems, with the exception of the power to the tail servo assemblies with controls in the neutral position. It is possible that the two systems are different here because of the larger control surfaces on the Puma that must accommodate greater aerodynamic forces.

Table 8. Comparison of RQ-11 Raven and RQ-20 Puma power requirements

| System Configuration | Power Required (W) | |
|---|---|---|
| | Raven | Puma |
| Flight control assembly neutral | 2.0 | 3.6 |
| Flight control servos active | 1.7 | 1.6 |
| Strobe lights on | 0.2 | 0.1 |
| Payload installed, off | 6.2 | 6.0 |
| Payload installed, on | 1.7 | 0.9 to 1.6 |

Proceeding from the assumption that system components between the two aircraft have similar power requirements, we presume that the idle power required by the motor of the Raven (which cannot be directly measured) is similar to the idle power required by the motor of the Puma (measured in Table 5) at 4.1 W. Subtracting this motor power (at 0% throttle) from the total power required by the Raven in its "tail and payload removed" configuration yields the power required for the remaining avionics equipment. In this case, subtracting an average motor power of 4.1 W from 8.9 W yields a power requirement of 4.8 W for the avionics and transmitter electronics of the Raven. We cannot, however, determine the power breakdown between the transmitter and other electronics.

Though the avionics are generally similar between the two aircraft, one difference between the two platforms that affects power requirements is the radio transmitter power.

The Raven has a maximum range of 10 km [29], and the Puma has a maximum range of 20 km [15]. Because the two systems use an identical ground control station and omnidirectional antennas, the difference in maximum range is most likely due to a difference in the transmitter amplifier power. Propagation losses in free space increase as a square of the distance; therefore, a transmitter with twice the range uses four times the power. For the purposes of this research, an assumption was made that the total transmitter power requirement of the Puma is roughly four times the power requirement of the Raven and that half of the power for the Raven's avionics assembly is for the transmitter. This means the avionics power electronics requirement is 2.4 W, transmitter power is 4(2.4 W) = 9.6 W, and total avionics subassembly power is 12.0 W for the Puma.

The total power required at any given point in the flight profile $P_{R,T}$ can be calculated as the sum of the power required for operating the flight controls $P_{controls}$, the payload $P_{payload}$, the avionics $P_{avionics}$, and the motor $P_{motor}$ as

$$P_{R,T} = P_{controls} + P_{payload} + P_{avionics} + P_{motor}\,. \tag{27}$$

The most conservative scenario (highest power demand) assumes that the SUAS is always operating in a mode with flight controls active, either to maintain an orbit or make slight attitude corrections. We also assume that the payload is always active and moving. Power used in operating the strobe lights and IR illuminator was measured to be negligible and is not incorporated in this model. The power requirements for deploying or stowing the payload is also not incorporated because of the short durations, each of which only occurs once each flight. Using the direct control and payload power measurements from Table 3, we used the avionics power calculated in the previous paragraph and the motor power from Table 5 to calculate the total power required from (27) as

$$P_{R,T} = (3.6+1.6)+(6.0+1.6)+12.0+P_{motor} = 24.8+P_{motor} \quad (\text{Watts})\,. \tag{28}$$

## 3. Flight Test and Observations

In this section, we explain the approach used to collect and analyze detailed flight performance data in support of building a model for flight performance simulation. After identifying relevant segments of data, probability distributions are used to ascertain relevant characteristics. Then a performance model is developed and validated.

### *a. Overview*

Detailed flight performance data was collected from a series of training flights performed at Camp Pendleton, CA in March 2018. The flights were conducted under the supervision of TALSA-West, the government contracted organization who provides training to Marines receiving their initial qualifications to operate the RQ-20 system. Flight performance data is automatically recorded by a ground control station when linked to an active aircraft and is available for immediate analysis in a rich text format at the conclusion of a flight. Obtaining the data in this form was assessed to be the most accurate and economical method of gathering precise throttle and performance metrics while the aircraft is in flight. For this research, we utilized flight data that was recoded from the four specific flights shown in Table 9 which can be considered representative of the takeoffs, landings, and typical airborne profiles that would be utilized by an operational unit.

Table 9. Flight data used for analysis

| Flight Segment | Date and Start Time | Total Duration (mins) | Surface Temp (°C) |
|---|---|---|---|
| 1 | Mar. 2, 2018 1346 | 35 | 37 – 39 |
| 2 | Mar. 5, 2018 1141 | 47 | 38 – 45 |
| 3 | Mar. 5, 2018 1505 | 11 | 40 – 42 |
| 4 | Mar. 6, 2018 1023 | 48 | 36 – 42 |

We began our analysis by plotting various attributes of the data to visualize the various flight profiles. This initially focused on characteristics like the aircraft's track over the ground shown in Figure 13 and relationships between altitudes and climb rate, as well as throttle and speed over time as illustrated in Figure 14.

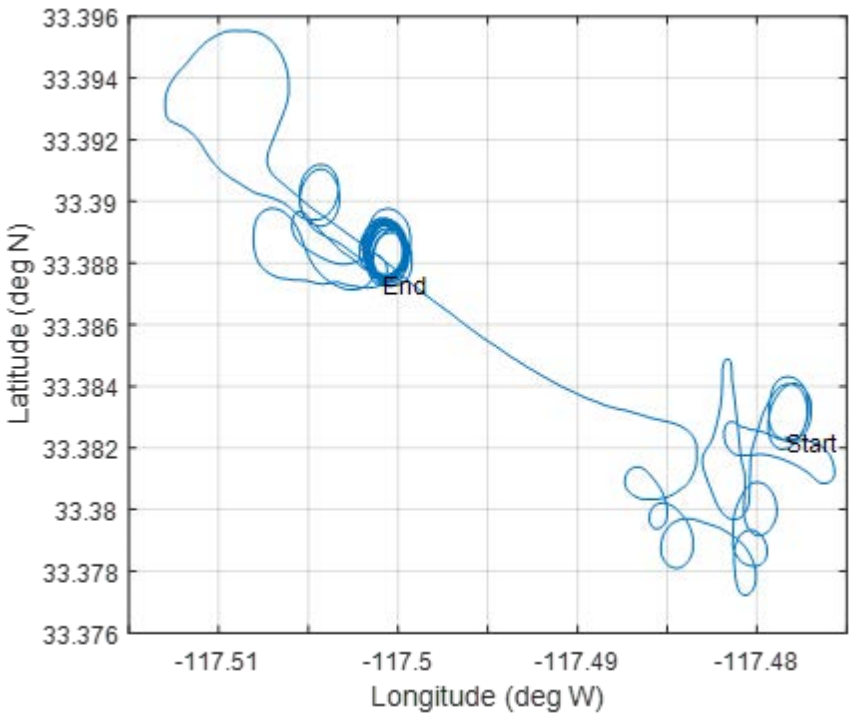


Figure 13. Geographic overview of fourth flight segment

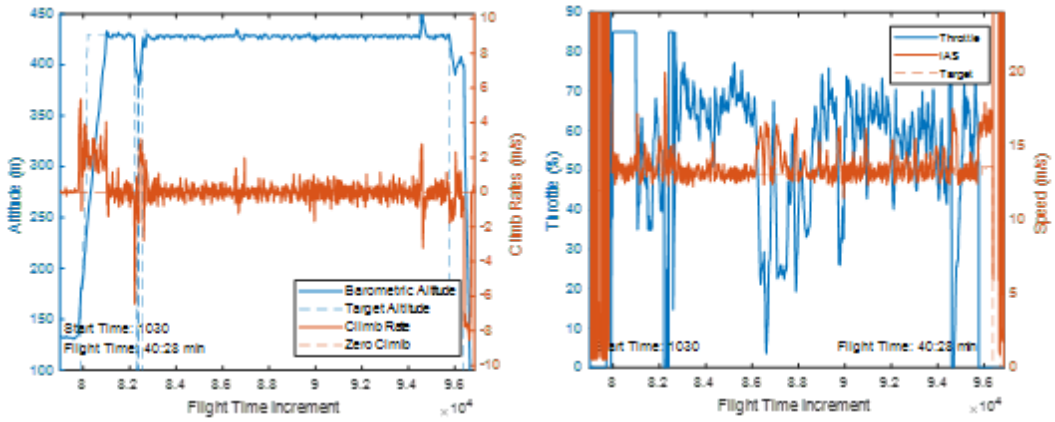


Figure 14. Plots of altitude/climb and throttle/speed, fourth flight segment

From these figures, we were able to identify general periods of time when the aircraft was in various profiles like climbing, descending, orbiting, or flying straight. From the altitude, throttle, and other flight data parameters, we also observed significant fluctuations in the data, meaning that the aircraft did not appear to maintain a stable throttle setting (or attitude configuration) over short time intervals even while it otherwise appeared

that the aircraft was attempting to maintain a constant altitude, airspeed, or some other parameter. While some variation was expected, the frequency and degree of the fluctuations differs significantly from the author's experience with manned flight in larger aircraft. The fluctuations can likely be explained by the smaller physical size and weight of the Puma, allowing it to be more dynamically affected by transient and unpredictable changes in winds or thermal updrafts. Also, the apparent precision of rate of change parameter measurements may show larger fluctuations within short time intervals that would appear smoother at a lower sampling rate. Lastly, it appears that the control laws used by the aircraft to maintain a profile are too reactive to momentary fluctuations, resulting in overdamping that causes frequent overcorrection and induced oscillations.

Because of this variability, we were unable to make straightforward measurements of throttle settings (which determine the power requirement) at a given airspeed or flight profile (climbing, turning, etc.). Available publications also do not provide specificity with which these various profiles should be flown or the goals of the flight control logic.

We determined the best approach to identify the throttle and flight attitude characteristics of each segment of flight was to identify a series of representative profiles from among the four flights and then compare the probability distributions of each variable of interest within the narrowly focused samples. By looking at a sufficient number of representative profiles, we assessed the mean characteristics and flight attitude parameters that are representative of each profile. We specifically identified the following profiles for closer study:

1. Straight and level, slow
2. Straight and level, fast
3. Straight climb
4. Straight descent
5. Level orbit
6. Climbing orbit
7. Descending orbit
8. Maneuvering

Of all the data collected, 58% was easily categorized into one of these profiles. Most of the remaining time was from when the aircraft was recording data but not actually flying or from short transitions between other phases of flight.

### *b. Identifying and Classifying Flight Segments*

To classify a specific flight segment, we isolated variable periods of time within each flight with similar characteristics by looking at a series of plots of aircraft parameters. For example, a straight leg is first characterized by a relatively straight line in the geographic overview shown in Figure 15. A straight leg additionally exhibits minimal variation in the aircraft's course and heading as illustrated in Figure 16. By contrast, for an orbiting segment, the geographic overview in Figure 17 exhibits a series of circular orbits of generally the same size and in the same direction. The course and heading in Figure 18 shows a generally continuous, gradual decrease over time with a discontinuity and jump from 0° to 359° as the aircraft course/heading passes through north on each orbit.

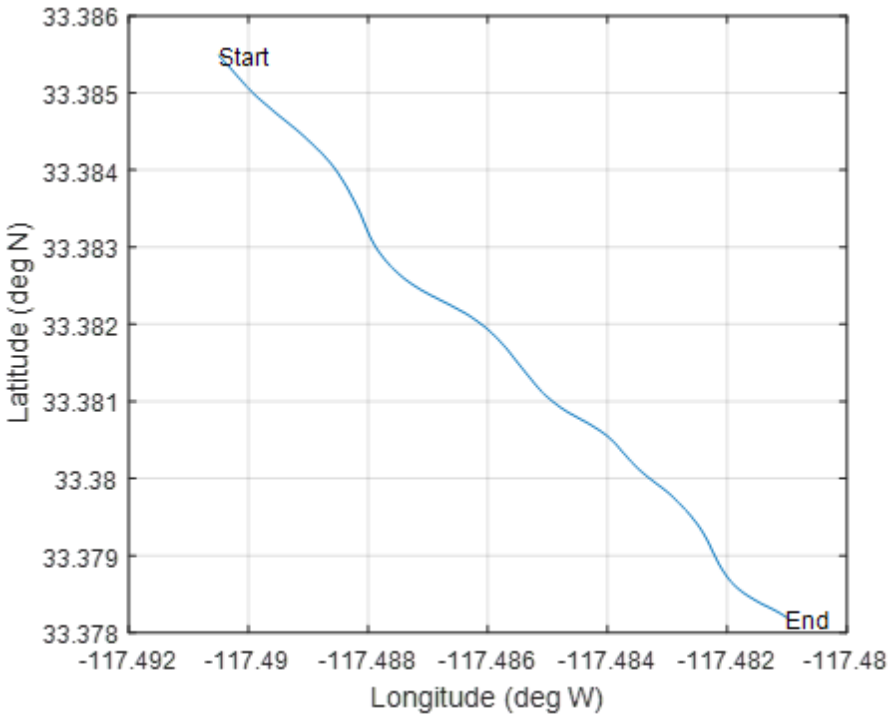


Figure 15. Geographic overview, first flight segment, start time 1352

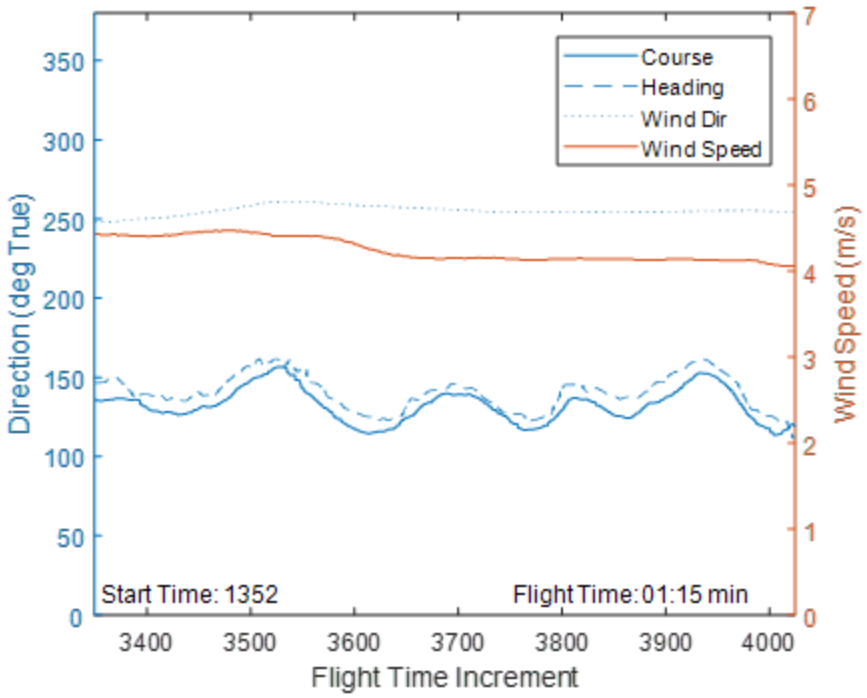


Figure 16. Course, heading, wind direction, and speed, start time 1352

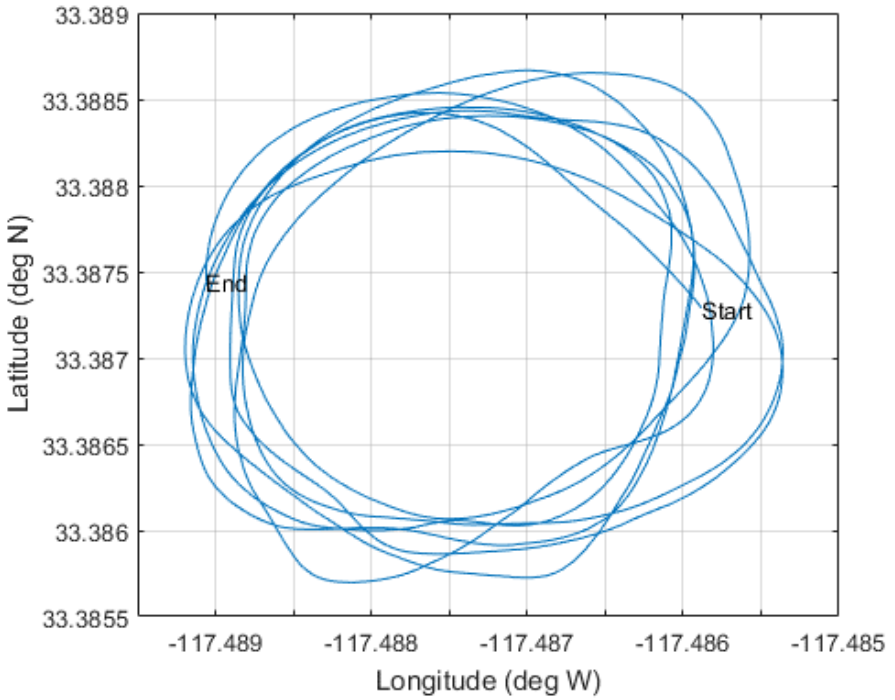


Figure 17. Geographic overview, second flight segment, start time 1202

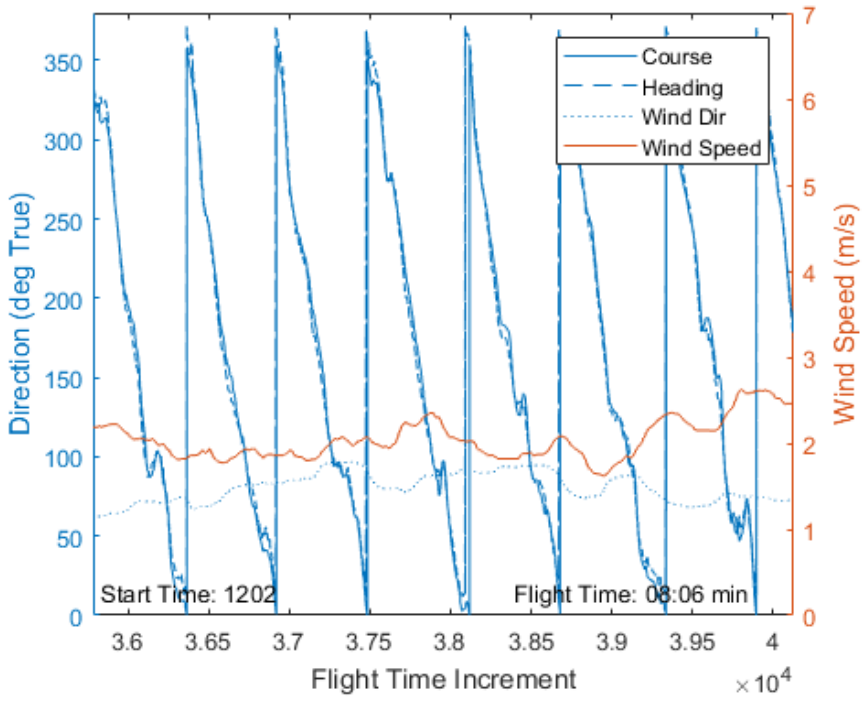


Figure 18. Course, heading, wind direction, and speed, start time 1202

To classify a segment as being level, we next looked at a plot of the targeted and actual altitude and climb rates over time as illustrated in Figure 19. From this illustration, we see that an altitude target of approximately 270 m is maintained, while the actual altitude fluctuates in a range of around 260 – 275 m over the measured period, indicating that the aircraft is attempting to maintain a level profile. The climb rate appears to have a mean of around zero, although frequent fluctuations of ±2 m/s occur.

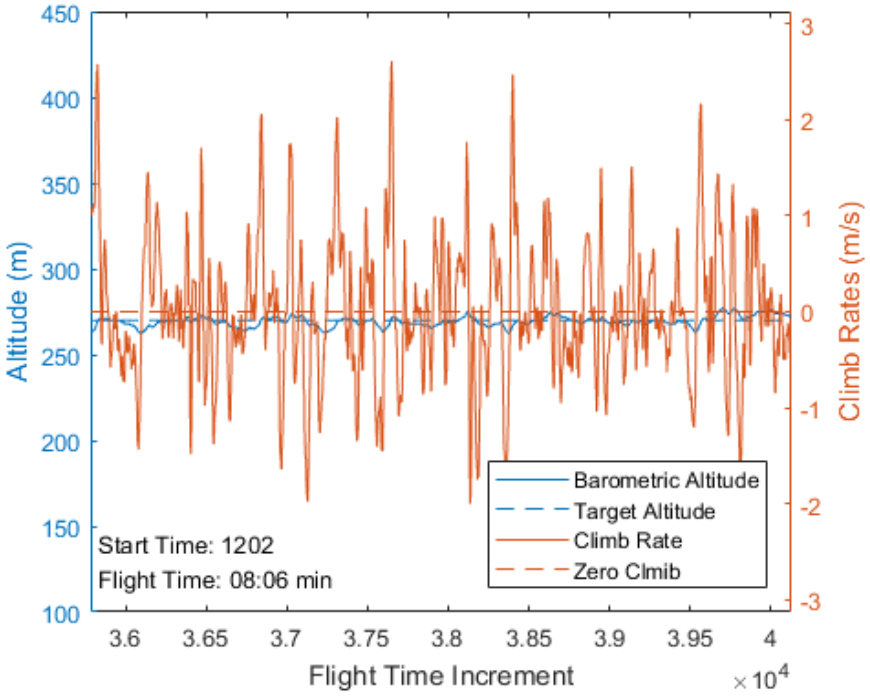


Figure 19. Altitude and climb rates, start time 1202

In contrast to a level segment, a climbing or descending segment like the one shown in Figure 20 is characterized by a steadily changing altitude toward a new target altitude and a climb rate, which, while it may still fluctuate, reveals a clear distribution either above or below the zero climb rate line.

For all profiles, we also sought segments that exhibited a consistent commanded speed. This was assessed by looking at a plot of indicated air speed (IAS) over time as shown in Figure 21, where we observe that a speed of 13 m/s is targeted throughout. The actual speed fluctuates from roughly 12 to 17 m/s during the period. Profiles with target speeds of 13 m/s were classified as slow; those at 21 m/s were classified as fast.

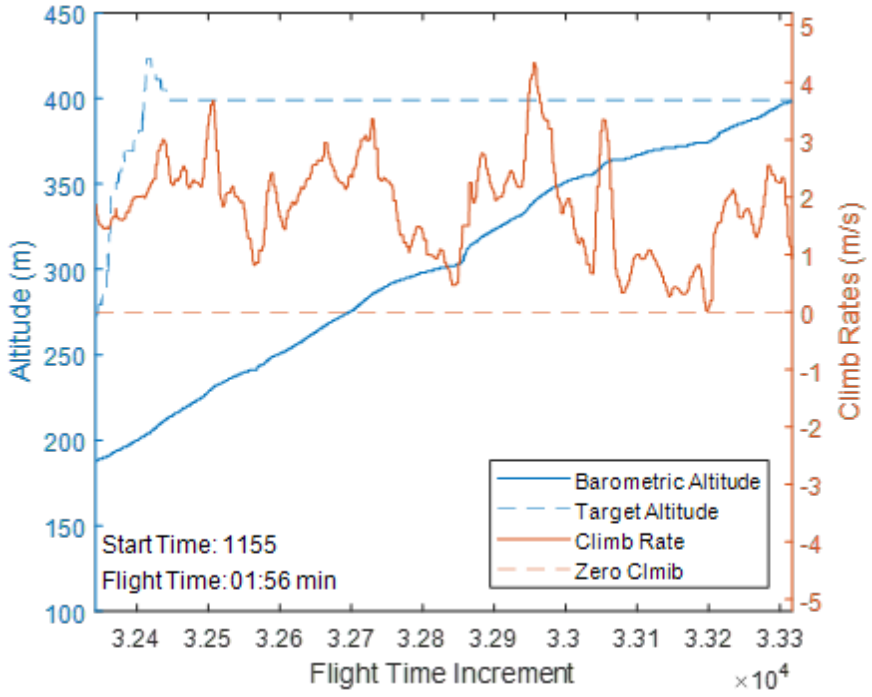


Figure 20. Altitude and climb rates, start time 1155

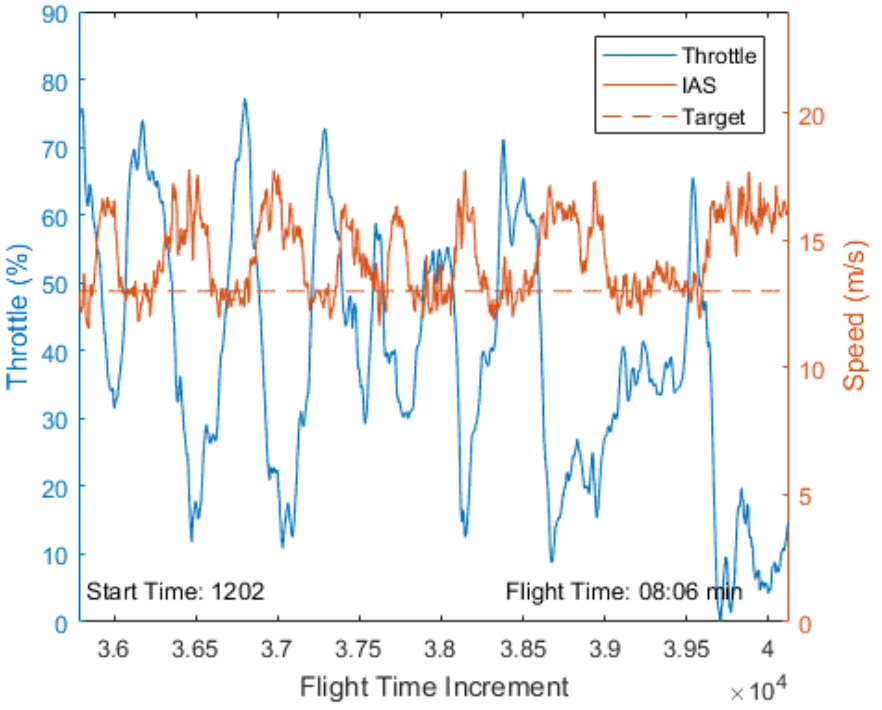


Figure 21. Speed and throttle, start time 1202

Portions of the flights were classified as maneuvering if they showed a series of turns in either direction, possibly intermixed with short periods of straight flight, as presented in Figure 22, while also maintaining a constant target altitude and speed.

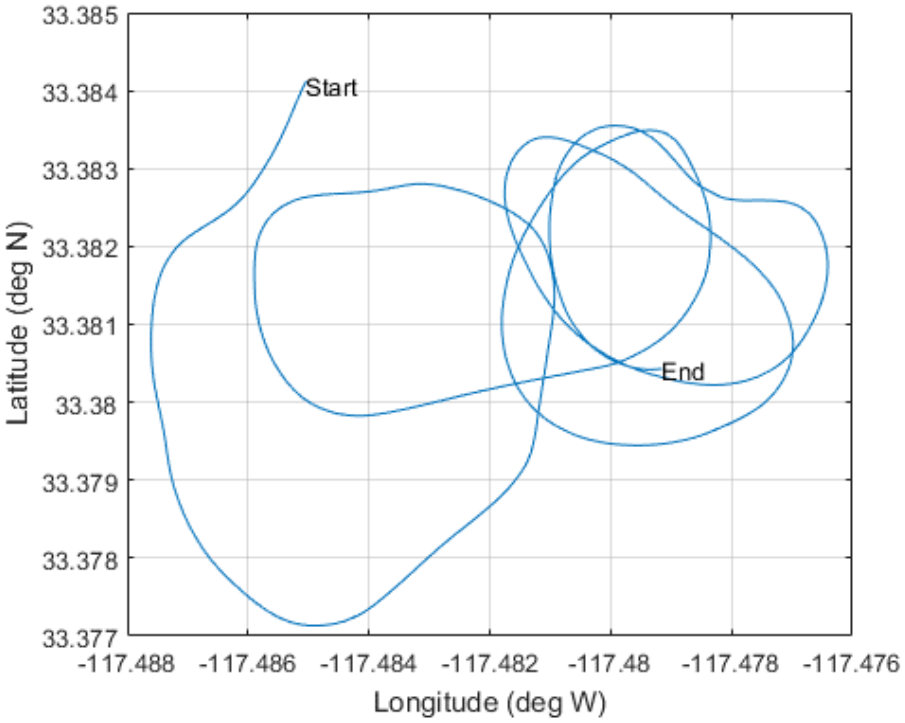


Figure 22. Geographic overview, first flight segment, start time 1415

### *c. Probability Distribution Calculations*

After all possible flight segments were identified and classified into a profile category, we plotted a series of probability distributions for each variable of interest within the sample. The variable of greatest interest for our research is the aircraft's mean throttle setting because this parameter directly corresponds to the power required by the aircraft. An example of this measurement is shown in Figure 23 where we can see the distribution of occurrences of each throttle setting alongside the plot of throttle settings versus time for the corresponding flight segment. Histogram bins are 5% wide, centered on multiples of five that correspond to the 5% intervals measured in Table 4.

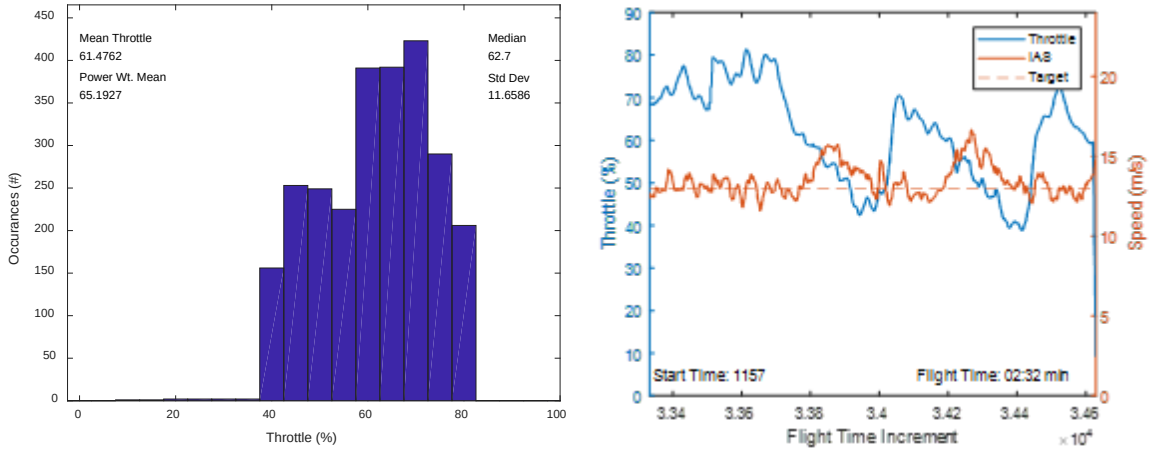


Figure 23. Throttle settings distributions, start time 1157

In this example, the throttle setting varies from around 40% to 80%, with a simple mean of 61.5%, median value of 62.7%, and standard deviation of 11.7. These three values are calculated, along with the histogram, to provide a feel for the distribution and variability of the data and to potentially identify flight segments that are outliers when compared to other similar segments of the same profile.

The throttle measurement of greatest interest is the Power Weighted Mean, a variable created to partially account for inefficiencies generated by the significant variability or fluctuations in the throttle over time. As we observed in Figure 11 and Table 5, there is an exponential relationship between the throttle and power. The difference in required power between 80% and 60% throttle is greater than the difference between 60% and 40% throttle. We, therefore, know that a mean between 80% and 40% underestimates the corresponding average power used between those two extreme states. To compensate for this, a weighting algorithm was devised through which the number of occurrences in each throttle histogram bin was first multiplied by the corresponding average power from Table 5. The cumulative total was then divided by the total number of observations to arrive at an average power for the sample. Using (26), we rendered this average power into a corresponding throttle percentage that yielded a power requirement. In other words, for the example shown in Figure 23, while a mean throttle of 61.5% may have been sufficient to maintain the desired altitude/speed combination for that segment of flight, the frequent

throttle fluctuations above and below that average means that a power corresponding to what would be required to maintain a 65.2% throttle was drawn from the battery over that time period to maintain the profile. This weighted mean is of primary importance in evaluating and predicting how the aircraft actually performs in the real world.

Similar to the throttle, we also analyzed parameters like speed, rates of climb or descent, and pitch for all flight segments to gain a comprehensive understanding of the aircraft performance and flight attitude. An example of this series of measurements is shown in Figures 24 to 26 for the same flight leg analyzed in the preceding paragraphs.

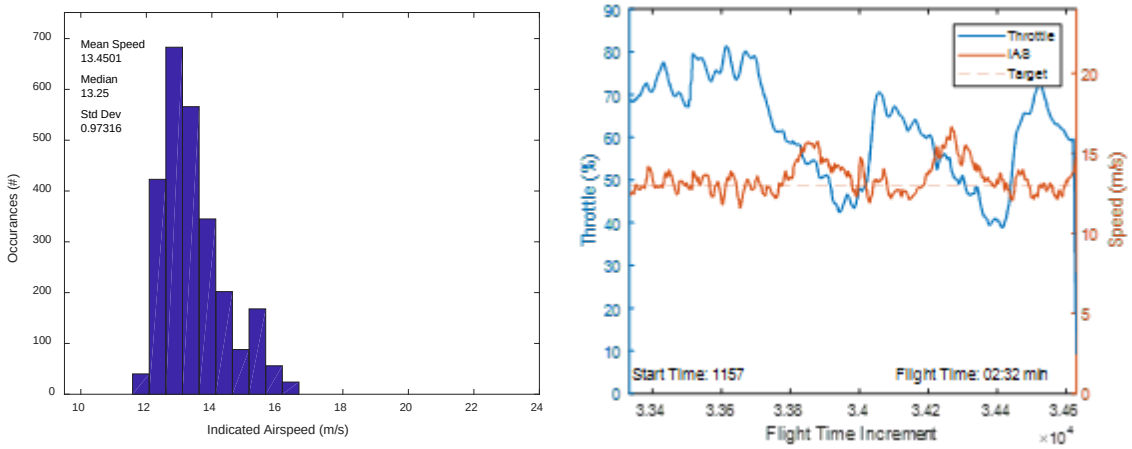


Figure 24. Indicated airspeed distributions, start time 1157

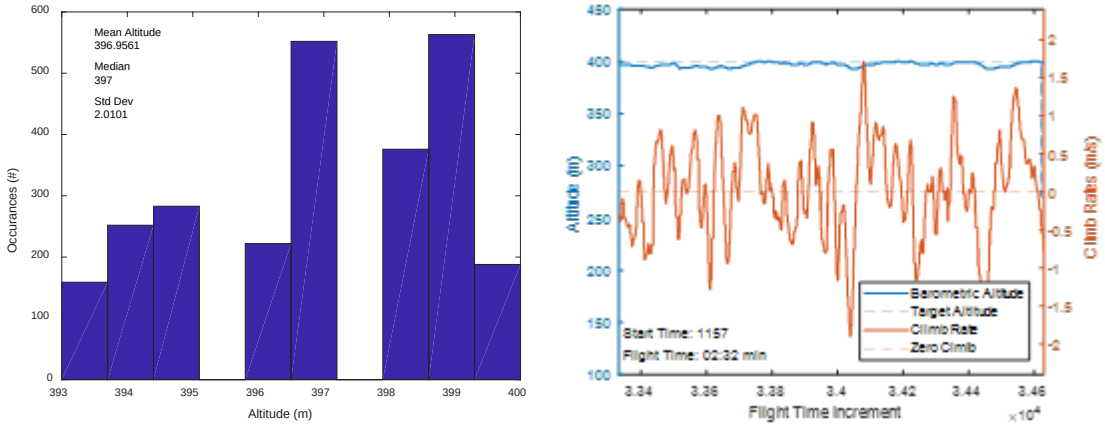


Figure 25. Altitude distributions, start time 1157

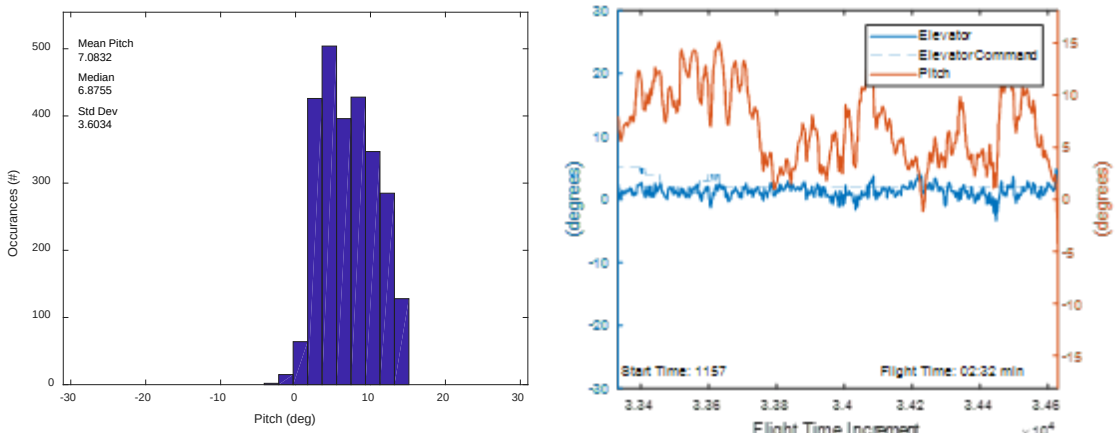


Figure 26. Pitch distributions, start time 1157

All flight segments identified as fitting each profile were analyzed in an identical fashion. A summary of the calculations are shown in Tables 10 to 17. Each line entry in a table represents a single flight segment from that profile. Each entry is uniquely identified by a flight number corresponding to the flights observed in Table 9 and the start time and duration of that segment. The mean of each set of observations is included alongside other statistics of interest to aid in identifying any outliers in the data. The line at the bottom of each table is a composite or average of the individual legs within the table, showing the total duration of all included lines and a weighted mean of each summarized parameter, weighted by the length of the individual segments. For example, from analyzing the entire 6 min 50 s of flight data from Table 10, we can calculate the overall weighted mean as 66.4 % throttle required for an actual speed of 13.2 m/s with a nose-up pitch of 7.6 degrees.

Table 10. Straight and level (slow) profile data

| Flight Information | | | Throttle (%) | | | | Speed (m/s) | | Altitude (m) | | Pitch (deg) | |
|---|---|---|---|---|---|---|---|---|---|---|---|---|
| # | Start | Length | Mean | Median | S.D. | Wt. Mean | Mean | S.D. | Mean | S.D. | Mean | S.D. |
| 1 | 1350 | 1:12 | 65.4 | 65.5 | 5.2 | 66.7 | 13.2 | 0.5 | 266.5 | 1.3 | 7.5 | 2.3 |
| 1 | 1355 | 0:18 | 63.2 | 62.6 | 2.4 | 64.1 | 13.2 | 0.8 | 304.4 | 0.9 | 6.3 | 1.8 |
| 1 | 1405[a] | 1:03 | 52.9 | 57.4 | 17.1 | 59.3 | 13.8 | 1.4 | 295.8 | 3.3 | 4.7 | 4.1 |
| 3 | 1510 | 2:44 | 64.3 | 64.1 | 3.8 | 65.7 | 13.2 | 0.4 | 394.0 | 1.1 | 7.3 | 1.8 |
| 4 | 1037 | 0:29 | 64.7 | 62.5 | 5.3 | 66.2 | 13.3 | 0.6 | 427.5 | 1.4 | 7.5 | 2.4 |
| 4 | 1043 | 2:07 | 65.6 | 66.6 | 5.5 | 67.4 | 13.2 | 0.5 | 427.7 | 1.0 | 8.2 | 2.1 |
| Composite | | 6:50 | 64.9 | | | 66.4 | 13.2 | | | | 7.6 | |

[a]Data from this leg appears to be an outlier and not included in composite.

Table 11. Straight and level (fast) profile data

| Flight Information | | | Throttle (%) | | | | Speed (m/s) | | Altitude (m) | | Pitch (deg) | |
|---|---|---|---|---|---|---|---|---|---|---|---|---|
| # | Start | Length | Mean | Median | S.D. | Wt. Mean | Mean | S.D. | Mean | S.D. | Mean | S.D. |
| 1 | 1356 | 0:17 | 51.9 | 51.9 | 15.2 | 57.4 | 21.4 | 0.8 | 308.4 | 3.8 | -2.4 | 3.5 |
| 1 | 1357 | 0:45 | 56.5 | 57.6 | 17.0 | 63.0 | 20.5 | 0.9 | 307.3 | 3.8 | -1.2 | 3.9 |
| 1 | 1406 | 0:42 | 62.7 | 66.7 | 11.8 | 66.5 | 20.5 | 1.0 | 297.8 | 1.9 | -0.4 | 3.4 |
| 1 | 1417 | 0:17 | 65.0 | 64.3 | 3.2 | 66.2 | 20.7 | 0.6 | 300.0 | 0.9 | -1.0 | 2.1 |
| Composite | | 2:01 | 59.2 | | | 64.1 | 20.7 | | | | -1.1 | |

Table 12. Straight climb profile data

| Flight Information | | | Throttle (%) | | | | Speed (m/s) | | ROC (m/s) | | Pitch (deg) | |
|---|---|---|---|---|---|---|---|---|---|---|---|---|
| # | Start | Length | Mean | Median | S.D. | Wt. Mean | Mean | S.D. | Mean | S.D. | Mean | S.D. |
| 1 | 1354 | 0:12 | 85.0 | 85.0 | 0.0 | 85.0 | 13.2 | 0.5 | 3.3 | 0.9 | 13.3 | 1.6 |
| 2 | 1155 | 1:49 | 85.0 | 85.0 | 0.0 | 85.0 | 13.0 | 0.6 | 1.7 | 0.9 | 12.0 | 1.9 |
| 2 | 1212 | 0:49 | 85.0 | 85.0 | 0.0 | 85.0 | 13.0 | 0.8 | 1.8 | 1.1 | 12.7 | 2.6 |
| 4 | 1033 | 0:33 | 85.0 | 85.0 | 0.0 | 85.0 | 13.2 | 0.3 | 2.1 | 0.7 | 14.1 | 0.9 |
| Composite | | 3:23 | 85.0 | | | 85.0 | 13.0 | | 1.9 | | 12.6 | |

During all climbs, we also observed (but did not include in the table) that when a climb was initiated, the throttle increased from wherever it was previously to 85.0% within one second of the altitude command change. The climb rate subsequently became positive within two seconds. Nearing the commanded altitude, the throttle automatically began to backoff starting around 7 to 8 m (typically 3 to 4 seconds) prior to reaching the intended altitude. From this backoff point, the throttle decreased in a linear manner from 85.0% to 65.0% with speed gradually reducing to around 12.7 m/s until the intended altitude was reached.

Table 13. Straight descent profile data

| Flight Information | | | Throttle (%) | | | | Speed (m/s) | | ROC (m/s) | | Pitch (deg) | |
|---|---|---|---|---|---|---|---|---|---|---|---|---|
| # | Start | Length | Mean | Median | S.D. | Wt. Mean | Mean | S.D. | Mean | S.D. | Mean | S.D. |
| 2 | 1200 | 1:59 | 0.0 | 0.0 | 0.0 | 0.0 | 16.0 | 0.6 | -1.2 | 1.0 | -0.5 | 2.2 |
| 2 | 1218 | 0:44 | 0.0 | 0.0 | 0.0 | 0.0 | 16.0 | 0.5 | -0.7 | 1.3 | -1.8 | 1.8 |
| Composite | | 2:43 | 0.0 | | | 0.0 | 16.0 | | -1.1 | | -0.9 | |

Table 14. Level orbit profile data

| Flight Information | | | Throttle (%) | | | | Speed (m/s) | | Altitude (m) | | Pitch (deg) | |
|---|---|---|---|---|---|---|---|---|---|---|---|---|
| # | Start | Length | Mean | Median | S.D. | Wt. Mean | Mean | S.D. | Mean | S.D. | Mean | S.D. |
| 2 | 1157 | 2:32 | 61.5 | 62.7 | 11.7 | 65.2 | 13.5 | 0.9 | 397.0 | 2.0 | 7.1 | 3.6 |
| 2 | 1202[a] | 8:06 | 38.3 | 37.4 | 18.8 | 46.3 | 14.3 | 1.5 | 269.4 | 2.9 | 3.0 | 3.8 |
| 3 | 1505 | 1:56 | 52.8 | 52.4 | 6.5 | 54.2 | 13.6 | 0.9 | 400.8 | 1.2 | 4.8 | 2.0 |
| 4 | 1034 | 1:52 | 49.6 | 48.7 | 9.8 | 52.1 | 13.7 | 0.9 | 428.7 | 1.7 | 4.0 | 2.8 |
| 4 | 1048 | 1:44 | 42.1 | 42.8 | 9.5 | 43.1 | 13.7 | 1.1 | 427.8 | 1.4 | 3.7 | 2.6 |
| 4 | 1050 | 15:00 | 58.8 | 60.6 | 9.1 | 61.4 | 13.5 | 0.7 | 427.8 | 1.2 | 6.5 | 2.5 |
| 4 | 1107 | 1:29 | 61.7 | 62.5 | 5.4 | 63.2 | 13.4 | 0.6 | 428.1 | 1.2 | 7.0 | 2.6 |
| Composite | | 24:33 | 58.2 | | | 59.1 | 13.6 | | | | 6.0 | |

[a]Data from this leg appears to be an outlier and not included in composite. Additional data from this leg not included in composite of Table 18 because of orbit radius (not shown).

Table 15. Descending orbit profile data

| Flight Information | | | Throttle (%) | | | | Speed (m/s) | | ROC (m/s) | | Pitch (deg) | |
|---|---|---|---|---|---|---|---|---|---|---|---|---|
| # | Start | Length | Mean | Median | S.D. | Wt. Mean | Mean | S.D. | Mean | S.D. | Mean | S.D. |
| 2 | 1201 | 0:52 | 0.0 | 0.0 | 0.0 | 0.0 | 16.0 | 0.6 | -1.4 | 0.9 | 0.2 | 2.2 |
| 3 | 1513[a] | 1:58 | 0.0 | 0.0 | 0.0 | 0.0 | 16.0 | 0.3 | -1.5 | 0.4 | -0.5 | 1.1 |
| Composite | | 2:50 | 0.0 | | | 0.0 | 16.0 | | -1.5 | | -0.1 | |

[a]Additional data from leg not included in composite of Table 18 because of orbit radius (not sown).

During descents, the throttle decreased to 0% within one second of the change in altitude command. Nearing the commanded altitude from above, the throttle increased 6 to 7 m above the desired altitude in a linear fashion to 75 to 85% over a 15 to 20 second period. In all observations, the aircraft passes through the desired altitude 4 to 6 s after the power begins to be applied, eventually overshooting the desired altitude by 9 to 10 m before levelling off and beginning a gradual climb back to the commanded altitude. During this process, the aircraft speed decreased in a linear manner form around 16 to around 13 m/s over about 10 s, holding close to 13 m/s until the desired altitude is reached.

Table 16. Climbing orbit profile data

| Flight Information | | | Throttle (%) | | | | Speed (m/s) | | ROC (m/s) | | Pitch (deg) | |
|---|---|---|---|---|---|---|---|---|---|---|---|---|
| # | Start | Length | Mean | Median | S.D. | Wt. Mean | Mean | S.D. | Mean | S.D. | Mean | S.D. |
| 2 | 1156 | 0:51 | 85.0 | 85.0 | 0.0 | 85.0 | 13.0 | 0.7 | 1.5 | 1.0 | 12.3 | 2.2 |
| 4 | 1033 | 0:25 | 85.0 | 85.0 | 0.0 | 85.0 | 13.5 | 0.4 | 1.9 | 0.6 | 14.8 | 1.0 |
| Composite | | 1:14 | 85.0 | | | 85.0 | 13.2 | | 1.6 | | 13.1 | |

Table 17. Maneuvering profile data

| Flight Information | | | Throttle (%) | | | | Speed (m/s) | | Alt (m) | | Pitch (deg) | |
|---|---|---|---|---|---|---|---|---|---|---|---|---|
| # | Start | Length | Mean | Median | S.D. | Wt. Mean | Mean | S.D. | Mean | S.D. | Mean | S.D. |
| 1 | 1407 | 7:38 | 66.4 | 71.2 | 18.4 | 72.6 | 20.1 | 1.4 | 306.1 | 4.1 | 1.4 | 4.9 |
| 1 | 1415 | 5:22 | 67.9 | 69.8 | 13.2 | 71.7 | 20.4 | 1.1 | 299.0 | 2.1 | 0.9 | 3.6 |
| Composite | | 13:00 | 67.0 | | | 72.1 | 20.2 | | | | 1.2 | |
| 1 | 1352[a] | 1:15 | 48.9 | 58.2 | 30.2 | 64.6 | 14.1 | 1.4 | 260.1 | 7.4 | 5.1 | 5.8 |
| 1 | 1358 | 6:23 | 37.5 | 36.7 | 26.0 | 54.0 | 14.6 | 1.6 | 305.3 | 7.7 | 3.0 | 5.6 |
| 2 | 1213 | 4:30 | 32.0 | 24.1 | 30.6 | 54.4 | 14.8 | 1.4 | 400.1 | 9.9 | 2.2 | 5.7 |
| 2 | 1219 | 3:33 | 32.9 | 27 | 29.3 | 51.7 | 14.8 | 1.6 | 398.2 | 8.3 | 2.7 | 5.0 |
| Composite | | 14:26 | 34.9 | | | 53.5 | 14.7 | | | | 2.7 | |

[a]Data from this leg appears to be an outlier and not included in composite.

In addition to the flight characteristics analyzed above, we also desired a more precise understanding of aircraft attitude characteristics during orbits or turns because SUAS typically spend a large amount of time in this profile. We specifically sought to identify turn rates and angle of bank (AOB) that corresponded to typical turn rates. Using the same analytical methodology explained earlier, we obtained the additional data summarized in Table 18 looking at the same orbiting legs identified in Tables 14 and 16.

Table 18. Additional flight orbit characteristics

| Flight Information | | | Turn | Turn Rate (deg/s) | | AOB (deg) | |
|---|---|---|---|---|---|---|---|
| # | Start | Length | Radius (ft) | Mean | S.D. | Mean | S.D. |
| 2 | 1157 | 2:32 | 310 | -7.7[a] | 4.4 | -10.3[a] | 6.8 |
| 3 | 1505 | 1:56 | 325 | -7.0 | 4.4 | -8.5 | 5.5 |
| 4 | 1034 | 1:52 | 345 | -7.5 | 5.1 | -9.2 | 7.1 |
| 4 | 1048 | 1:44 | 325 | -7.7 | 3.4 | -9.9 | 5.4 |
| 4 | 1050 | 15:00 | 325 | -8.0 | 4.3 | -10.9 | 6.0 |
| 4 | 1107 | 1:29 | 310 | -8.4 | 3.4 | -11.6 | 5.7 |
| 3 | 1513 | 1:58 | 325 | -7.6 | 4.2 | -11.6 | 6.8 |
| 2 | 1156 | 0:51 | 310 | -8.8 | 4.6 | -13.2 | 9.9 |
| 4 | 1033 | 0:25 | 345 | -8.0 | 3.9 | -11.5 | 7.6 |
| Composite | | 27:47 | 325 | -7.9 | | -10.4 | |

[a]Negative values indicate left-hand turn direction.

For comparison, we summarized the key parameters for each of our flight profiles in Table 19 using the "weighted mean throttle" as our representative throttle reference.

Table 19. Summary of flight profiles

| Profile Name | Speed (m/s) | Throttle (%) | Rate of Climb (m/s) | Pitch (deg) |
|---|---|---|---|---|
| Straight and level, slow | 13.2 | 66.4 | 0.0 | 7.6 |
| Maneuvering, slow | 14.7 | 53.5 | 0.0 | 2.7 |
| Level orbit | 13.6 | 59.1 | 0.0 | 6.0 |
| Maneuvering, fast | 20.2 | 72.1 | 0.0 | 1.2 |
| Straight and level, fast | 20.7 | 64.1 | 0.0 | -1.1 |
| Straight climb | 13.0 | 85.0 | 1.9 | 12.6 |
| Climbing orbit | 13.2 | 85.0 | 1.6 | 13.1 |
| Straight descent | 16.0 | 0.0 | -1.1 | -0.9 |
| Descending orbit | 16.0 | 0.0 | -1.5 | -0.1 |

This comparison allows us to draw some interesting observations. First, all flight profiles at the slow speed and all climbs stay fairly close to the 13.8 m/s (±0.9) reference, fast profiles were close to 20.4 m/s (±0.3), and descents were at 16.0 m/s.

Second, the throttle required for straight and level, slow flight is actually slightly greater than the throttle required for fast flight, a result that initially appears counterintuitive. Upon further examination, this effect is most likely due to the Puma operating on what is known as the "back side of the power curve" when it is in the slow flight profile. The generic drag curve (also known as the power curve because of motor power being required to overcome drag) depicted in Figure 27 shows the aerodynamic relationship between an aircraft's speed and required power while in flight. At slower speeds, greater induced drag at a high angle of attack (AOA) and pitch leads to an increased power requirement. At faster speeds accompanied by a lower AOA and pitch, power requirements increase due to increasing parasitic drag. The application of this theory to explain our initial observations of the Puma's slow and fast power requirements are further corroborated by two additional pieces of evidence. First, we note that the Puma tends to fly slightly faster at 13.6 m/s when orbiting than when flying level at 13.2 m/s, using 7.3% less throttle at the slightly faster speed. In the maneuvering profile at 14.7 m/s, the throttle is

lower still by an additional 5.6%. Second, although we cannot directly measure the Puma's AOA, the aircraft pitch clearly shows a decrease from the slow profile to the fast profile, suggesting a rightward move on the power curve.

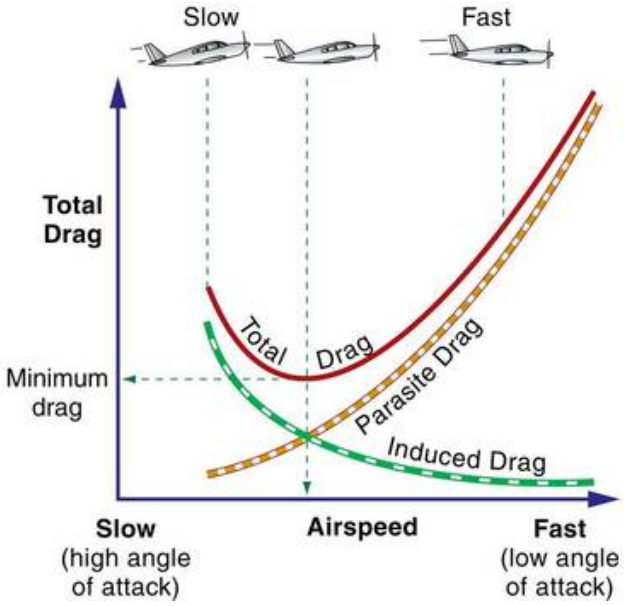


Figure 27. Generic aircraft power (drag) curve. Source [30].

Lastly, we observed that all climbs or descents used the same power regardless of flying straight or maneuvering. The maneuvering, as would be expected, increases the drag on the aircraft, causing climbs with maneuvering to occur at a lower climb rate; descents with maneuvering were at a slightly higher descent rate.

### *d. RQ-20 Flight Performance Model*

Since we lacked the ability to generate detailed performance data across a broader spectrum of speeds and flight environments, it was not possible to generate something like a performance chart that is common in traditional aerodynamic analysis and prediction models. From the data we compiled, we put together a comprehensive performance summary in Table 20 that simplifies the information above.

Our model sought to consolidate similar profiles around the throttle requirement because accounting for aircraft power is the focus of this research. We chose one straight

and level profile because fast and slow flight yielded nearly the same power consumption. Speed and pitch characteristics are noted in Table 20 because they are relevant in later sections. The orbiting and slow maneuvering profiles were combined because they are also similar in speed, throttle, and pitch and could be used interchangeably in a similar portion of a flight model. When flying over an objective, there is generally not an operational need to orbit or maneuver at a high speed; therefore, we choose not to incorporate a separate fast maneuvering profile into the model. All climbs were modeled together and all descents together because speed, rate of climb/descent, pitch, and throttle requirements were similar.

Table 20. RQ-20 flight performance model

| | St. and Level (slow or fast) | Descending | Orbit or Maneuvering | Climbing |
|---|---|---|---|---|
| Speed (m/s) | 13.2 or 20.7 | 16.0 | 14.4 | 13.1 |
| Throttle (%) | 65.3 | 0.0 | 56.3 | 85.0 |
| Rate of Climb (m/s) | 0.0 | -1.1 | addl. -0.35 | 1.9 |
| Pitch (deg) | 7.6 or -1.1 | -0.5 | 4.3 | 12.9 |
| Turn Rate (deg/s) | | | +/- 7.9 | |
| AOB (deg) | | | +/- 10.4 | |

### *e. Typical Flight Profiles*

To validate our data collection, analysis, and performance modeling to this point, we chose to apply our performance estimates to possible aircraft operational profiles to see if our performance and flight endurance forecasts matched manufacturer specifications and operator experience. We generated three generic flight profiles based on our knowledge of actual mission sets [3] which cover a broad range of possible aircraft uses. The first profile chosen is a local security mission where the aircraft orbits near the takeoff point until landing. The second profile is a one-way route that might be used for route reconnaissance ahead of a convoy or to ferry an aircraft to another location or user. The last profile chosen, incorporating aspects of the other two, is an out-and-back mission where the aircraft flies to a mid-range objective, orbits for a period of time, then returns to the origin point to land.

All profiles in Table 21 to 23 begin with a fully charged aircraft battery (25.2 V) assuming negligible time and power loss during preflight checks before launch. The

starting energy capacity of the battery is calculated with (22). At the takeoff time, the aircraft conducts a straight climb until reaching a typical cruising altitude of 500 ft (152 m) AGL. At a typical climb rate of 1.9 m/s, this takes 1.3 min (0.022 hrs) at a constant throttle of 85%. The enroute or loitering times of each profile were adjusted so that the aircraft can descend from altitude and land as the battery is reaching its low voltage threshold. From 500 ft, this takes 2.3 min (0.038 hrs) at a constant throttle of 0%. The total power calculations are based on (24), incorporating the $P_{motor}$ from (22).

Table 21. Local security mission flight profile

| Profile | Time (hr) | Throttle (%) | Total Power (W) | Energy (Wh) |
|---|---|---|---|---|
| Starting Capacity of Battery | | | | 297.0 |
| Takeoff and Climb | 0.022 | 85.0 | 508.4 | -11.2 |
| Orbit/Maneuvering | 2.134 | 56.3 | 133.5 | -284.9 |
| Descent and Land | 0.038 | 0.0 | 24.8 | -0.9 |
| Total | 2.194 | | | 0.0 |

Table 22. One-way route flight profile

| Profile | Time (hr) | Throttle (%) | Total Power (W) | Energy (Wh) |
|---|---|---|---|---|
| Starting Capacity of Battery | | | | 297.0 |
| Takeoff and Climb | 0.022 | 85.0 | 508.4 | -11.2 |
| Straight and Level | 1.436 | 65.3 | 198.4 | -284.9 |
| Descent and Land | 0.038 | 0.0 | 24.8 | -0.9 |
| Total | 1.496 | | | 0.0 |

Table 23. Out-and-back flight profile

| Profile | Time (hr) | Throttle (%) | Total Power (W) | Energy (Wh) |
|---|---|---|---|---|
| Starting Capacity of Battery | | | | 297.0 |
| Takeoff and Climb | 0.022 | 85.0 | 508.4 | -11.2 |
| Straight and Level | 0.382 | 65.3 | 198.4 | -75.7 |
| Orbit/Maneuvering | 1.000 | 56.3 | 133.5 | -133.5 |
| Straight and Level | 0.382 | 65.3 | 198.4 | -75.7 |
| Descent and Land | 0.038 | 0.0 | 24.8 | -0.9 |
| Total | 1.824 | | | 0.0 |

From these basic profile summaries and power estimates, we see that the local security mission has the longest operational duration of 2 h 12 min, the one-way mission has the shortest duration of 1 h 30 min, and the out-and-back profile had a duration of 1 h 49 min. These times do not include the 10 to 15 min reserve that is available below the low voltage indication at 18.8 V. Including the time in the low voltage region still does not bring the aircraft's performance under this model very close to the manufacturer's rated three hour [13] endurance limit, but the model does perform closely to the two hour limit that actual system operators witness in an operational environment [3], [31]. We believe it is safe to conclude that our performance model accurately reflects aircraft performance.

This performance model and the three flight profiles detailed here are employed in Chapter IV under a variety of solar conditions to estimate the aircraft performance with PV augmentation.

## B. SOLAR CELLS AND WING CONFIGURATION

### 1. Cell Selection, Efficiency, and Performance

The solar cell chosen for this research is the FG-SM12-11: 8.3W (6V) Solar Submodule produced by Global Solar Energy, Inc. shown in Figure 28. This submodule contains a prefabricated array of twelve cells connected in series.

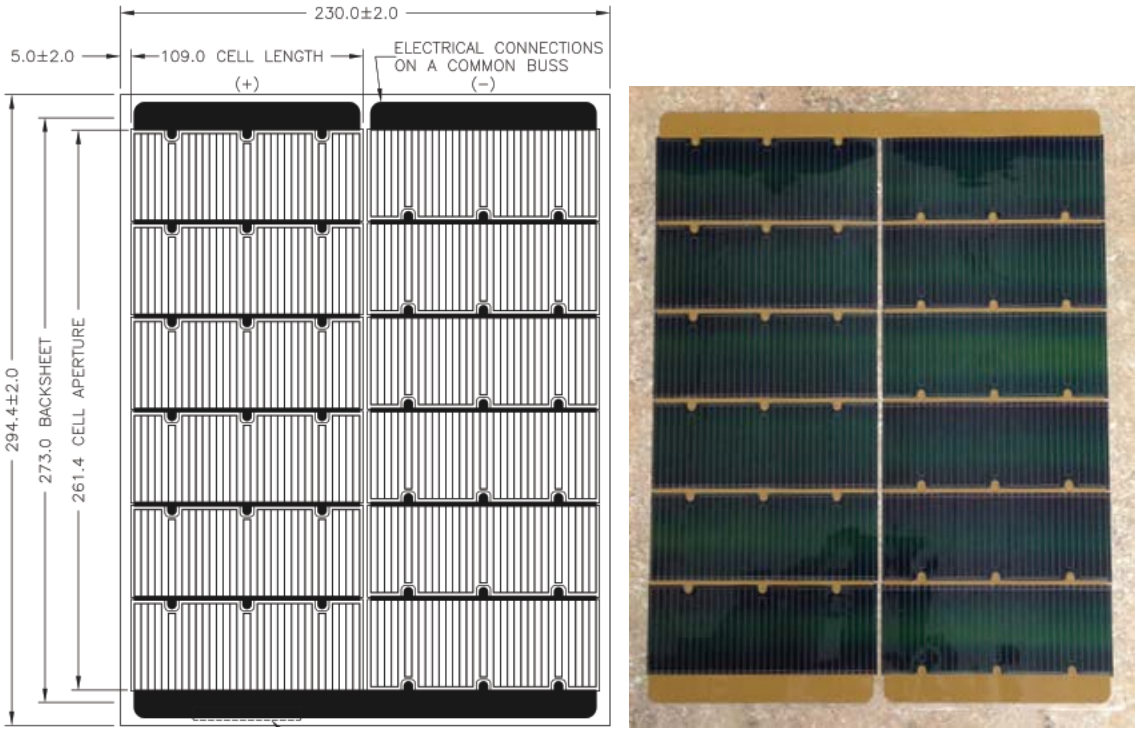


Figure 28. Dimensions [in mm] (left) and photo (right) of FG-SM12-11 Solar Submodule. Source [32], [25].

A flexible TFPV solution is necessary in this application in order for the PV array to conform to the contour of the aircraft's airfoil on the top surface of the wing, which has a slight curvature. This specific submodule also provides a relatively high efficiency compared to other flexible cells. Additionally, it is relatively inexpensive compared to other alternatives [10] and is already available in sufficient quantities having been used in previous NPS research. Based on the rated power and aperture area provided by the manufacturer, shown in Table 24, this cell submodule can provide an efficiency as high as 14.5% [25].

Table 24. Features of FG-SM12-11 Solar Submodule. Adapted from [32].

| Physical Characteristics | |
|---|---|
| Overall Dimensions (mm) | 230 × 294 × 0.29 |
| Aperture Dimensions (mm) | 220 × 261 |
| Aperture Area ($cm^2$) | 574 |
| Weight, grams | 32 |
| Power to Weight Ratio (W/kg) | 260 |

Testing completed at NPS in 2017 [10] evaluated a number of sample submodules to determine actual performance parameters. Testing of electrical characteristics was performed using the Amprobe SOLAR-600 Power Analyzer and concluded that the actual performance was nearly identical to the specifications provided by the manufacturer. These results are summarized in Table 25.

Table 25. Electrical characteristics for the FG-SM12-11 Solar Submodule. Adapted from [32] and [10].

| Parameter | Product Specification | Measured |
|---|---|---|
| $V_{OC}$ (V) | 8.0 | 7.86 |
| $I_{SC}$ (A) | 1.4 | 1.55 |
| $V_{MP}$ (V) | 6.4 | 6.17 |
| $I_{MP}$ (A) | 1.3 | 1.33 |
| $P_{MAX}$ (W) | 8.3 | 8.21 |
| Efficiency (%) | 14.5 | 13.8 |

Calculations in the remainder of this research are based on the observed cell efficiency of 13.8%. Unless otherwise specified, this efficiency based on actual measurements is assumed to remain constant with negligible changes in cell temperature from changing outside air temperature and aircraft altitude.

### 2. Wing Area and Cell Coverage

The wing of the RQ-20 Puma has three main sections: a center wing and two outer wing segments. Each section provides a flat surface for mounting an array of individual solar cell submodules connected in series. This research replicates a design shown in Figure 29, which maximizes the usable surface area of the wing while preserving the integrity of the chosen PV submodule.

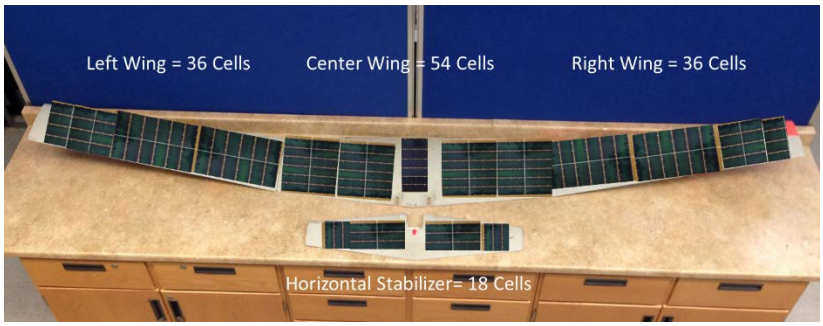


Figure 29. Solar panels layout on wing and horizontal stabilizer. Source [25].

Based on the conclusions of previous research into the optimum granularity of MPPT application [25], the design used in this research does not include the addition of a solar array on the horizontal stabilizer as depicted in Figure 29. The specifications of the final layout chosen are detailed in Table 26.

Table 26. Wing area and PV cell configuration. Adapted from [25].

| | Wing Dimensions (cm) | | | Solar Array | | |
|---|---|---|---|---|---|---|
| | Length | Width | Area ($cm^2$) | Submodules | Cells | Aperture area ($cm^2$) |
| Outer Wings | 89 | 19-28 | 2086 | 3 | 36 | 1722 |
| Center Wing | 102 | 28-36 | 2856 | 4.5 | 54 | 2583 |
| Total | - | - | 7028 | 10.5 | 126 | 6027 |

## C. SOLAR RADIATION CALCULATIONS

### 1. Sample Environments

The impact of PV augmentation depends a great deal on the region and time of year, which affect how much solar irradiance is available to the system. To address the range of environments, we chose three locations to closely replicate the best, average, and worst-case scenarios of likely USMC operations.

A South China Sea location, around 20º N latitude, has similar characteristics to the Hawaiian Islands and North Africa during peak summertime conditions with ample sunlight and is our best-case scenario. The United States location, around 35º N latitude, has similar characteristics to much of the Middle East and Korea during a time of year with

approximately equal amounts of light and darkness and serves as an average scenario. The Northern Europe location, around 55º N latitude, in winter conditions with very little direct sunlight, reflects a worst case. Unless otherwise stated, this research assumes clear skies, meaning that the full benefit of direct irradiance is accounted for in all calculations of solar insolation.

### 2. Effect of Time of Day

In any given environment, the amount of solar irradiance, based on the solar elevation angle, can also vary a great deal over the course of a day. This is illustrated in Figures 30 and 31 for the three chosen locations, hereafter referred to simply as the best, average, and worst cases. In the best-case scenario, the sun is above the horizon for 13.5 hours, reaching a peak elevation of 86.5º and producing a maximum irradiance of 1.02 kW/m$^2$. By contrast, in the worst-case example, the sun is above the horizon for only 7.0 hours, reaching a peak elevation of 11.6º and producing a maximum irradiance of 0.54 kW/m$^2$.

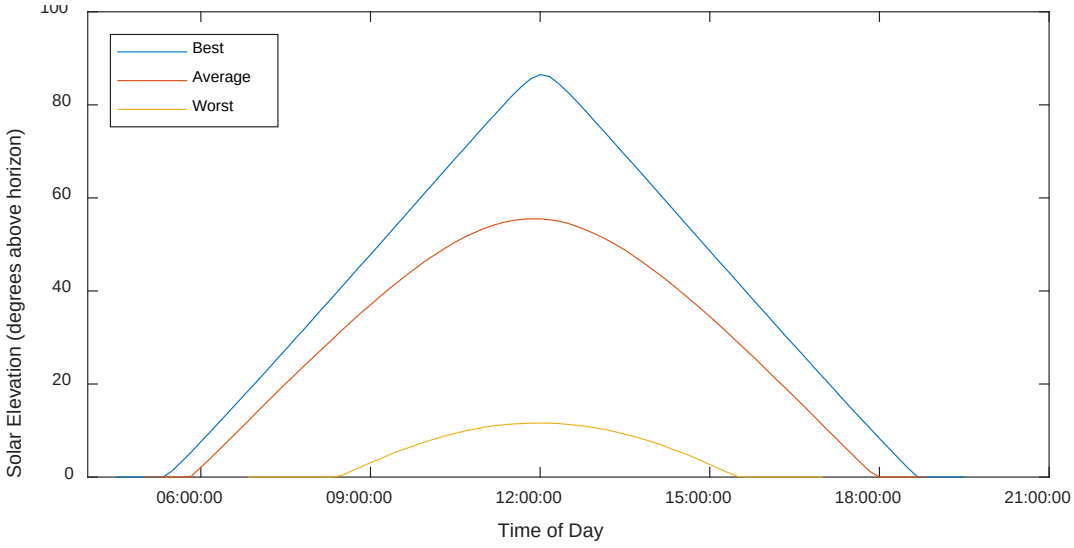


Figure 30. Daily solar elevation for selected locations

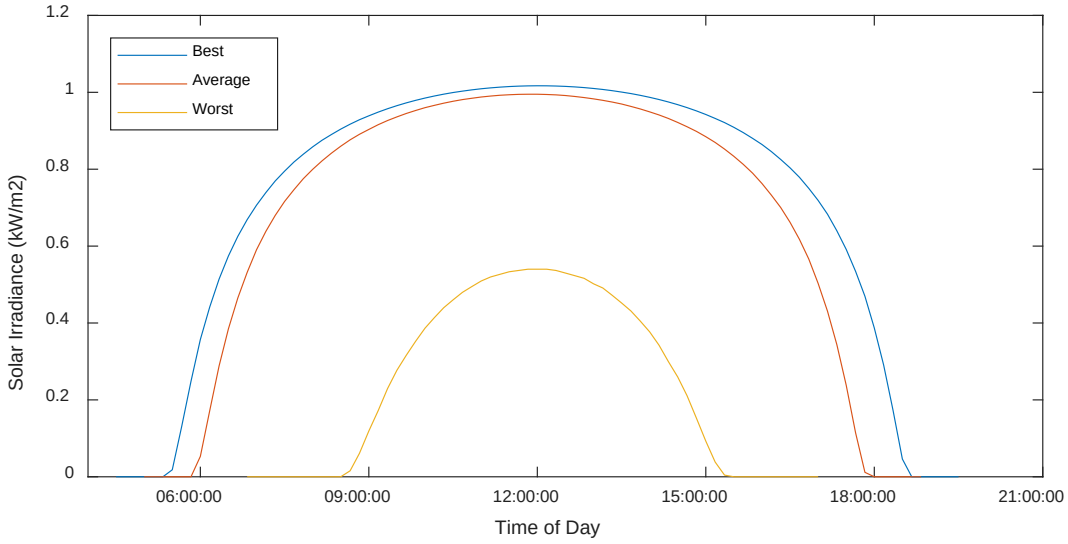


Figure 31. Daily irradiance for selected locations

## D. INTEGRATION OF POWER HARDWARE

Two main power electronics components are required with our PV augmentation system. The first is a combination MPPT and boost converter. Previous research [7] utilized a Genasun GV-4 boost converter with a rated efficiency of 99% and a measured actual efficiency from 96–98%. Initially weighing 6.5 oz, the component weight was reduced to 3.6 oz with the outer case removed. The GV-4 is incompatible with the higher voltage requirements of the Puma battery; however, the Genasun GVB-8 [33] is compatible and appears to be identical in rated efficiency, size, and weight to the version of the GV-4 evaluated in 2010.

The second component required is a battery balancer charger. We chose to use the Ultra-Balancer from Common Sense RC, which has been tested in previous NPS research and also recommended by engineers with Naval Air Warfare Station China Lake [7]. This component is expected to have negligible impact on overall system power.

## E. EFFECT OF ADDED WEIGHT ON POWER REQUIREMENTS

We also considered the possible impact of our proposed PV system components on the overall aircraft weight. We proposed the addition of a total of 10.5 FG-SM12-11 solar

submodules, three Genasun GVB-8 MPPTs with cases removed, and a battery balancer. The weights and subtotals of these components are summarized in Table 27.

Table 27. Weights of PV system components

| Component | Quantity | Weight (oz) | Subtotal (oz) |
|---|---|---|---|
| Solar Submodule [10] | 10.5 | 1.13 | 11.9 |
| MPPT [7] | 3 | 3.6 | 10.8 |
| Battery Balancer [7] | 1 | 0.5 | 0.5 |

The total weight of all subcomponents added is 23.2 oz. This equates to 10.4% of the present basic aircraft weight of 14 lbs. The aircraft manufacturer does not clearly publicize any type of weight limits or cargo capacities for this this aircraft as the aircraft is not designed for any type of transport. Fortunately, we were able to consult with personnel responsible for completing composite repairs on the aircraft, and they stated that a 10 to 20% weight addition to the aircraft is acceptable [28]. The 10% addition of weight that we desire for PV cells and power electronics should, therefore, be acceptable for overall performance.

The aircraft is also presently rear-heavy and has a center of lift that is 1 to 2 inches in front of the avionics bay [28]. Adding a small amount of weight to the front of the avionics bay, as we propose with the addition of our power electronics, helps move the aircraft center of gravity farther forward. The avionics bay on the RQ-20 has around 1170 $cm^3$ of empty space that is more than sufficient for the proposed hardware. This forward shift in CG has the side effect of shifting aircraft weight closer to the center of lift, increasing stability, therefore, there should be no stability concerns from the weight addition in the avionics bay.

## F. COST ESTIMATES

To balance the economy of the proposed PV augmentation system, it is helpful to consider the approximate subcomponent costs. Table 28 is included to summarize the current costs of the individual components in the proposed system. The total cost as currently designed, not including any labor or installation expenses, is $749 per aircraft.

Table 28. Costs of PV system components

| Component | Quantity | Price ($/ea.) | Subtotal ($) |
|---|---|---|---|
| Solar Submodule [10] | 10.5 | 18 | 189 |
| MPPT [33] | 3 | 150 | 450 |
| Battery Balancer [7] | 1 | 30 | 30 |
| Misc. Hardware[a] [7] | 1 | 80 | 80 |

[a]Protection film, connectors, wiring, tape

THIS PAGE INTENTIONALLY LEFT BLANK

# IV. SIMULATION RESULTS

In this chapter, we incorporate the measurements, equations, and models produced in previous chapters into a series of computer simulations of RQ-20 flight endurance with a PV array. First, we analyze the impact of various individual flight modes like turning or level attitude flight on PV output. Next, we integrate those conclusions into simulations of an entire flight profile. Subsequently, we investigate the potential impact of changes to the existing flight control algorithm.

## A. IMPACT OF PV CELLS DURING AIRCRAFT MANEUVERS

### 1. Efficiency

The amount of solar irradiance captured by the PV array and usable by the aircraft's systems is restrained by a series of component inefficiencies. First, we must account for a reduction due to the incidence angle between the surface normal of the panel and the sun. Next, we consider the efficiency of the PV cells in converting the light into electrical energy. Then, the electrical system MPPT and DC-DC converter add further losses before power is finally available to power system components. If power is available to charge the battery, there are added losses converting the electrical energy into chemical storage. The losses from the specific components used in our system are summarized in Table 29.

Table 29. Summary of system component efficiency

| Component | Efficiency Factor |
|---|---|
| Panel Incidence Angle | cos($i$) |
| Solar Submodule [10] | 13.8% |
| MPPT [7] | 96-98% |
| Battery Charge or Discharge [6] | 90% (81% total) |

The total efficiency for a PV panel of any size can be summarized as

$$\eta_{total} = (0.138)(0.97)\cos(i) = 0.134\cos(i)\,. \tag{29}$$

We can further visualize the total system efficiency as a function of the incidence angle in Figure 32. From any combination of environmental conditions, the overall

percentage of solar energy that can be harnessed steadily decreases from a high of 13.4% as the incidence angle increases.

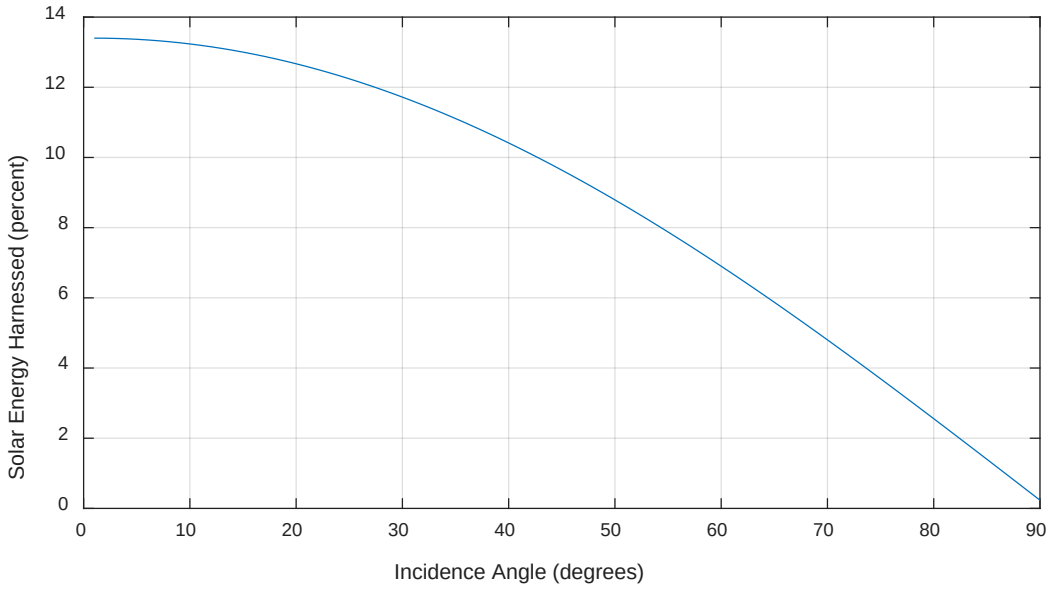


Figure 32. Solar energy harnessed as a function of incidence angle

### 2. Level Flight

In level flight, we wanted to know if the total power generated by the PV array on the RQ-20 Puma displayed any variations based on the aircraft heading because of the slight 10° dihedral on the outer wings. The magnitude of this effect is illustrated in Figure 33 and shows the total power delivered to the Puma in accordance with (18) at an altitude of 1 km in mid-latitude summer conditions. Three profiles are illustrated with high (85°), medium (40°), and low (15°) sun angles as the relative azimuth from the sun to the tail of the aircraft rotates through a full 360°. It is clearly evident from Figure 33 that the aircraft heading has no impact on the power delivered from the PV array.

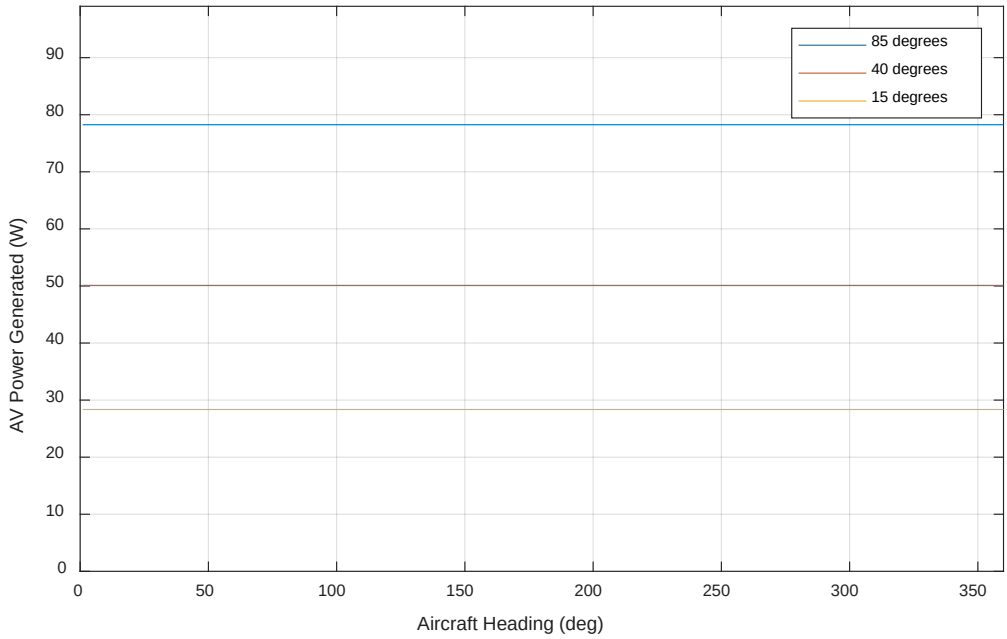


Figure 33. RQ-20 PV array performance in level flight

### 3. Turning Flight

Due to the wing dihedral, we expected a more pronounced effect on power generation based on aircraft heading while in a turn with an AOB. This variation is illustrated in Figure 34 using the same altitude, environment, and sun angles used for Figure 33 but with the aircraft in a sustained 10.4° AOB. The variation based on aircraft heading is most pronounced at lower sun angles, though a minor variation is still apparent even when the sun is almost directly overhead. There is additionally a slight flattening of the power curve at the lowest sun angle when the relative azimuth is around 240 to 300°; this is the period when the aircraft is banking away from the sun, where all three panels have the greatest incidence angle and the effect of diffuse irradiance dominates.

The average power through the turn for the 40° profile is 49.5 W, occurring at azimuths of 180° and 360°. The average of 77.1 W for the 85° profile occurs at the same headings. The average power through the turn for the 15° profile is 28.4 W, occurring at azimuths of 2° and 178°, skewed slightly because of the “flattening” effect noted earlier. It helps to note the point where average values occur to assist with modeling and simulation of aircraft performance over the course of a dynamic flight profile. Since we assume that

an aircraft spends roughly equivalent amounts of time at every heading during a period of circular orbiting, we model the aircraft attitude during this portion of a flight at one of the average points, greatly simplifying the potential complexity of our model.

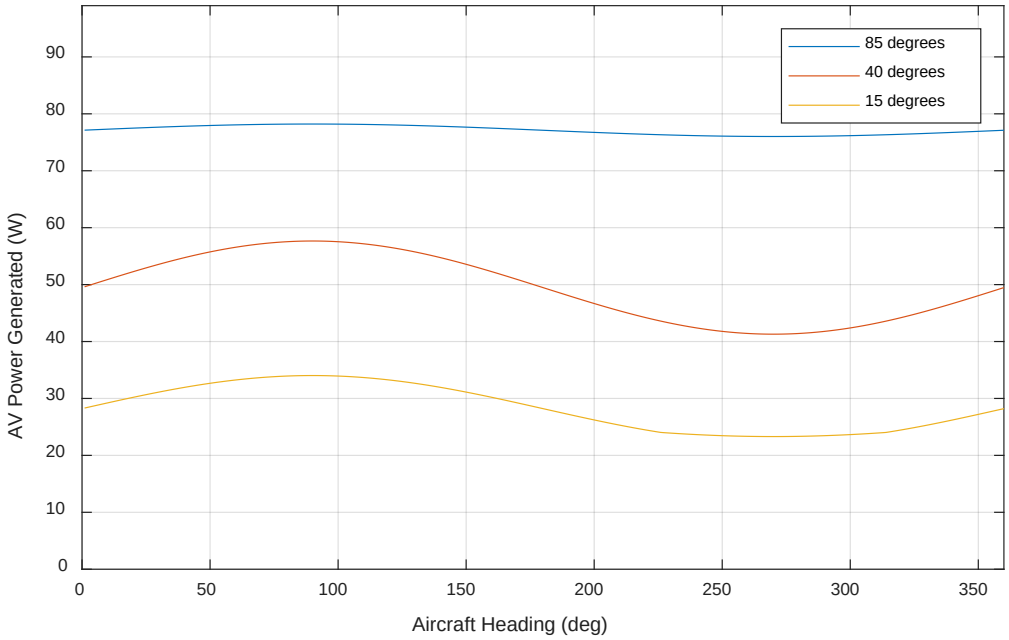


Figure 34. RQ-20 PV array performance in turning flight

### 4. Altitude Effects

The component of direct atmospheric transmittance is affected by the altitude of the aircraft or PV array above the surface of the earth. At higher altitudes, there is less atmosphere through which the solar radiation has to pass; therefore, there is less attenuation and scattering of the solar energy and direct transmittance is higher. Since the density of the atmosphere is also greatest closer to the surface, the largest gains are observed in the lowest six kilometers of the atmosphere [24]. This relationship is illustrated in Figure 35 based on (10) and (11) using a mid-latitude summer environment. Figure 35 is oriented with the dependent variable of altitude on the vertical axis to a maximum altitude of 2 km (6562 ft) MSL and highlights an altitude band of typical RQ-20 operations from 500 to 1500 ft. Direct transmittance is also dependent on the angle-of-incidence; the three samples shown demonstrate the impact of this variable from high (85°) to low (15°) sun angles.

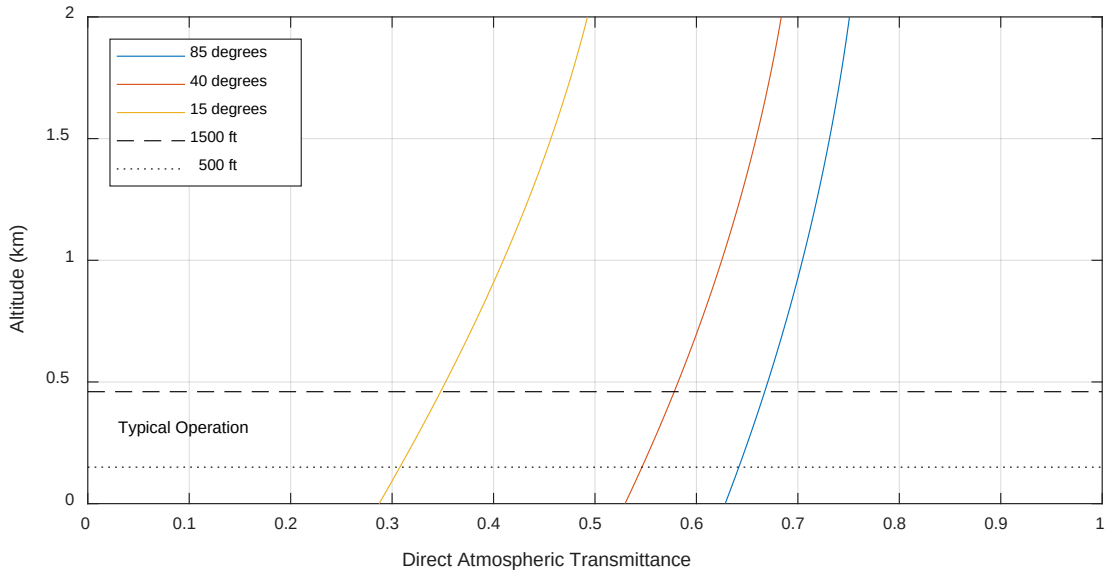


Figure 35. Direct atmospheric transmittance as a function of altitude

## B. IMPACT OF PV CELLS ON FLIGHT PROFILES

From our review of the level and turning flight profiles earlier in this chapter, we observe that as long as the sun is not very low to the horizon, average PV output remains roughly the same whether the aircraft is flying level or in a steady turn. This is a significant observation in simplifying our assessment of the impact of the PV array on our possible flight profiles. Since our most likely profiles all consist primarily of either straight and level or orbit/maneuvering flight, we expect that power generation benefits from a PV array remain the same for all mission types whether flying straight or orbiting. For this reason, we chose to use a basic out-and-back profile like the one described in Table 23 for all subsequent comparisons and analysis unless otherwise specified. The out-and-back profile has a flight duration between the extremes of the other two and covers all the types of flight that we assessed as worthy of investigation.

Any additional variation in the benefits of a PV array should solely be from the selected flight altitude, geographic location, and the time of day of the flight. We cover a range of possible locations through comparison of the three specific environments and times of year presented in Figure 31.

### 1. Effect of Takeoff Time

A flight during the early morning (or late afternoon) still provides performance gains to a PV augmented aircraft, though the gains are not as substantial as during the middle of the day. This is because the sun is at lower elevation angles in the morning (or afternoon), resulting in higher AM-levels and less irradiance. The results of a simulation of aircraft battery energy consumption for flights in different environments beginning at 0830 hrs (sunrise in the worst case scenario) are shown in Figure 36 and Table 30.

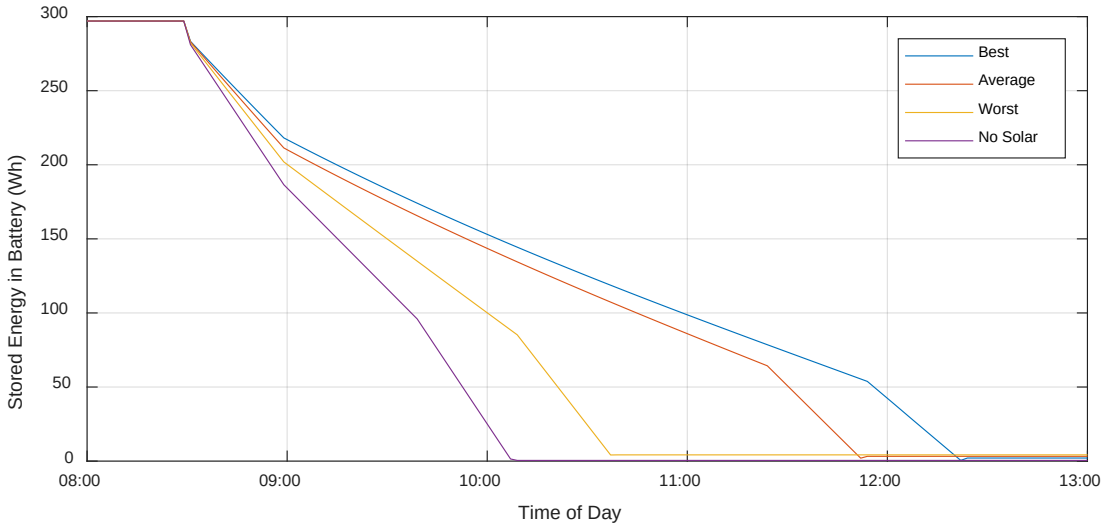


Figure 36. Flight duration with early takeoff, 500 ft MSL

These simulations reveal that the PV augmented aircraft operating at a less than ideal part of the day gains between 28 minutes and 2 hours and 15 minutes of additional flight time, up to a 136% improvement. In all four cases, the aircraft is flying an identical profile but the rate of energy loss from the battery, illustrated by the slope of the lines in Figure 36, is clearly smallest in the best-case environment due to higher sun elevations in that environment. It is also notable that the rate of change is not linear. In the best-case environment, as seen in Figure 36, while flying the same orbiting portion of the flightplan, 50 Wh of energy is lost from the battery between 09:15 hrs and 10:04 hrs (49 min), another 50 Wh between 10:53 hrs and 11:52 hrs (59 min). We expect this relationship as the sun rises to higher elevations close to local noon, providing greater power through the PV array.

Table 30. Flight duration with early takeoff, 500 ft MSL

| Profile | Flight Duration (hrs:min) | Increase (hrs:min) | Improvement (%) |
|---|---|---|---|
| Baseline, no solar | 1:39 | | |
| Worst Case | 2:07 | 0:28 | 28 |
| Average Case | 3:23 | 1:44 | 105 |
| Best Case | 3:54 | 2:15 | 136 |

Knowing that the PV array provides the most power to the aircraft during the middle of the day when the sun elevation is highest, we model flights around this factor. The simulations shown in Figure 37 and Table 31 reflect the same environments and profiles used before with takeoff times of PV-augmented flights adjusted to coincide with the peak-sun elevations in each environment. These simulations indicate that the PV augmented aircraft gains between 33 minutes and 2 hours and 45 minutes of additional flight time, up to a 157% improvement. As before, the rate of energy loss from the battery decreases in our best-case scenario and is at a minimum in all environments during the middle of the day.

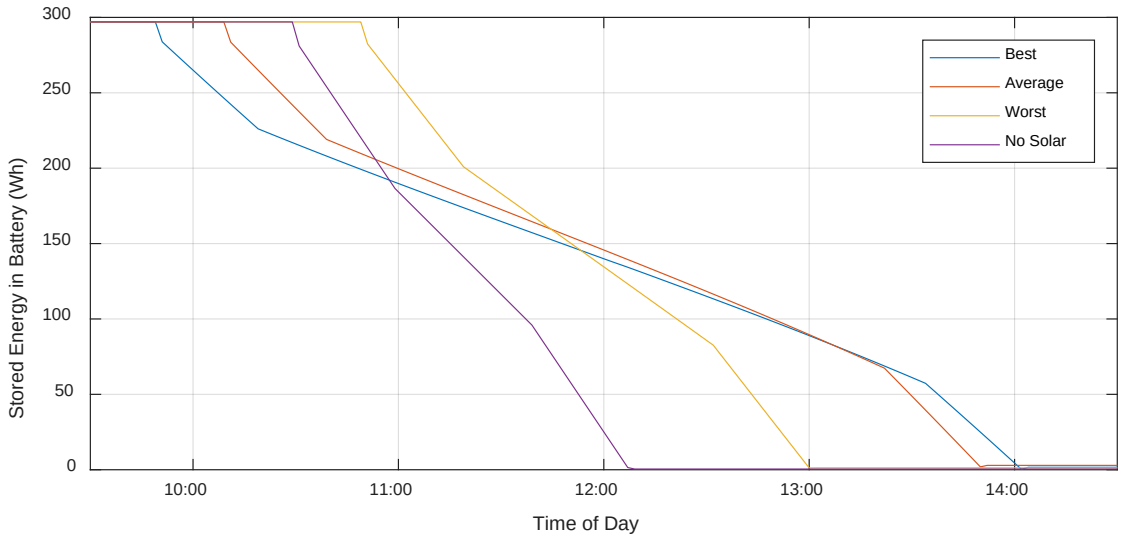


Figure 37. Flight duration with mid-day takeoff, 500 ft MSL

Table 31. Flight duration with mid-day takeoff, 500 ft MSL

| Profile | Flight Duration (hrs:min) | Increase (hrs:min) | Improvement (%) |
|---|---|---|---|
| Baseline, no solar | 1:39 | | |
| Worst Case | 2:12 | 0:33 | 33 |
| Average Case | 3:42 | 2:03 | 124 |
| Best Case | 4:14 | 2:35 | 157 |

### 2. Effect of Flight Altitude

The effects of aircraft altitude on the output of a PV array discussed earlier in this chapter were also simulated with our aircraft model in average environmental conditions. This simulation builds on the relationships illustrated in Figure 35 by accounting for the added costs of flight time at a relatively high climb power setting (85% throttle) to reach an altitude more ideal for the PV array. The simulation of varying flight altitudes shown in Figure 38 and Table 32 also accounts for the increasing amounts of time from each altitude that an aircraft is able to descend with a 0% throttle setting, consuming less total power than required for the avionics and payload, to allow a moderate amount of battery recharging during the descent before landing. All simulations were conducted during the middle part of the day to observe the maximum effect in an average environment. Improvements in flight duration of up to 37 minutes or 17% (from the already PV-augmented baseline of 3:42) were observed as the aircraft increased its operating altitude from 500 ft to 4,500 ft MSL. Above 4,500 ft, the added power loss from a longer initial climb could not be overcome by the additional output from the PV array; performance improvements were less than at a lower altitude.

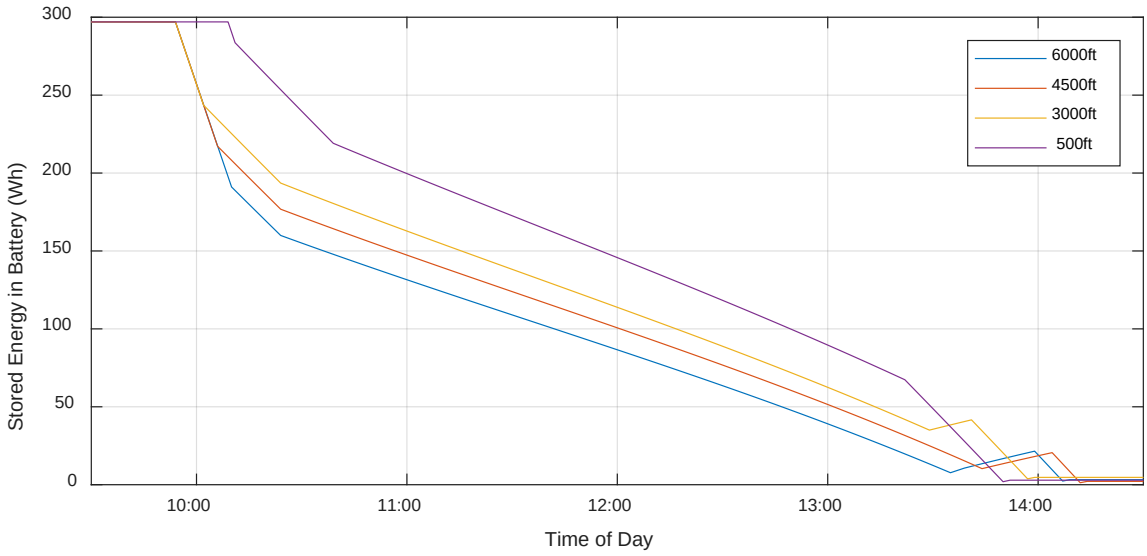


Figure 38. Flight duration in average environment, varying altitude

These simulations initially suggests an optimum operating altitude of around 4,500 ft MSL for an aircraft taking off at sea level but does not account for all potential considerations. The constraints of the aircraft payload determine from what altitude the aircraft can still accomplish the assigned mission with an acceptable degree of accuracy. A typical mission involving target tracking, identification, or surveillance with an EO/IR optic is less effective from higher altitudes. A mission to provide radio relay or EM detection may benefit from a higher elevation. Winds also play an important factor in aircraft flight performance, especially for small aircraft at lower operating speeds. Since winds tend to be stronger at higher altitudes, operating higher can significantly help or hurt range and groundspeed.

Table 32. Flight duration in average environment, varying altitude

| Profile | Flight Duration (hrs:min) | Increase (hrs:min) | Improvement (%) |
|---|---|---|---|
| 500 ft MSL | 3:42 | | |
| 3,000 ft MSL | 4:04 | 0:22 | 10 |
| 4,500 ft MSL | 4:19 | 0:37 | 17 |
| 6,000 ft MSL | 4:14 | 0:32 | 14 |

This analysis also did not have the ability to observe or test aircraft performance at altitudes above 1,500 ft MSL. Our model makes an assumption that climb performance remains constant through at least 6,000 ft. In reality, the climb performance of aircraft gradually decreases with an increase in altitude due to a number of aerodynamic factors, though these effects are generally less noticeable below 6,000 ft.

## C. IMPACT OF CHANGES TO FLIGHT TTPS

Clear benefits to aircraft endurance are available with the addition of a PV array. Our analysis to this point also identifies a couple of areas of the aircraft operating model that may be optimized to further improve endurance or that would improve endurance even without a PV array. The first of these optimizations is to adjust the aircraft's standard cruise and maneuvering speed to the point of minimum drag as illustrated in Figure 27. Based on interpolations of the relationship between throttle and speed in Tables 10, 11, 14, and 17, an aircraft speed around 15 m/s should require around 53% throttle, a 12% reduction from the current requirement for straight cruise flight and a 6% reduction in the throttle requirement for orbiting flight.

The second proposed optimization is an adjustment to aircraft flight control algorithms to deliberately fly specific throttle and attitude settings for a given profile, making adjustments much less frequently than what is presently observed. This optimization avoids the frequent chasing of precise speed, altitude, and rates of climb, favoring a constant throttle and allowing slight altitude and speed deviations within moderate limits. This change should tighten the distribution of throttle settings used to fly a given profile, aligning our "weighted mean" more closely with the arithmetic mean. Based on our closest consistent observations to a 15 m/s target speed in Table 17, this control algorithm change could further reduce the throttle requirement of 53% to somewhere above 35%. A midpoint of 44% throttle reduces the total aircraft power requirement for level flight to only 80.8 W.

This optimized power requirement is less than half the current requirement. The power savings from this optimization is also greater than the power benefit from a PV array in most sunlight conditions. The benefits of these effects are illustrated in Figure 39 and

Table 33 based on a takeoff time to maximize flight during mid-day and operations in ideal environmental conditions.

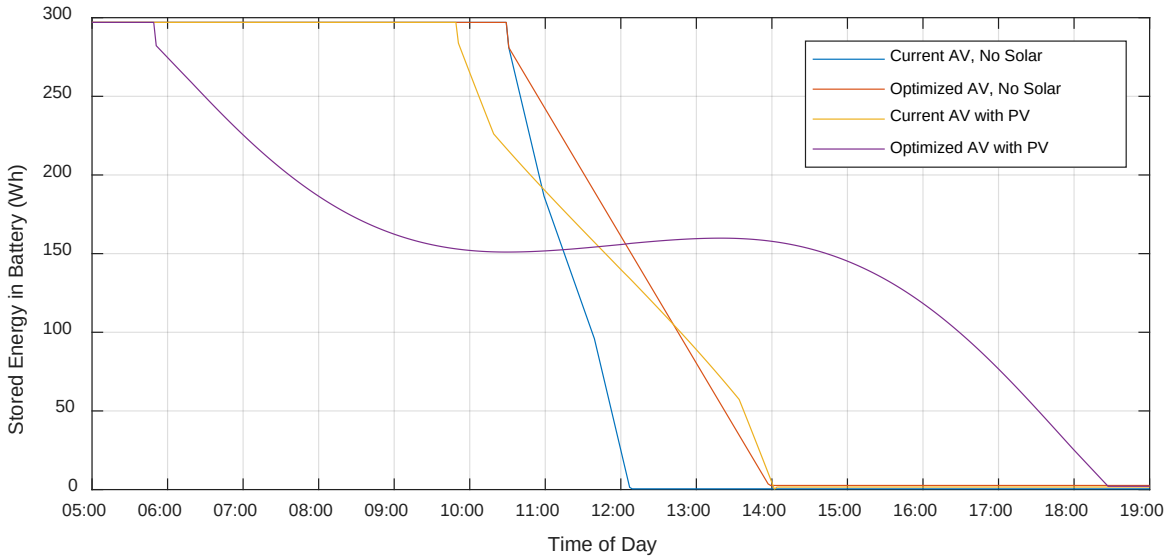


Figure 39. Optimized AV flight duration, mid-day takeoff, 500 ft MSL

The optimized AV is able to more than double its flight duration relative to the baseline AV in the current configuration. The synergistic combination of a PV array with the optimized performance parameters yields substantial benefits. For a period of three hours around mid-day, the PV array is actually able to power the entire AV and charge the battery while in flight. Throughout the remainder of the flight, excess power consumption for the AV above what the PV array is able to provide is so low that the flight can extend from within 15 minutes after sunrise to 15 minutes before sunset.

Table 33. Optimized AV flight duration, mid-day takeoff, 500 ft MSL

| Flight Duration | No Solar (hrs:min) | With PV Array (hrs:min) |
|---|---|---|
| Current AV | 1:39 | 4:14 (+ 2:35 or 157%) |
| Optimized AV | 3:29 (+ 1:50 or 111%) | 12:39 (+ 11:00 or 667%) |

THIS PAGE INTENTIONALLY LEFT BLANK

# V. CONCLUSION AND RECOMMENDATIONS

## A. SUMMARY

In this research, we began by identifying a significant limitation in a widely employed system that can be mitigated with the addition of new TFPV technology. A comprehensive survey of relevant technical aspects of the problem and recent related research identified specific commercially available technology to use that provides the greatest benefit at a reasonable cost and weight.

Our original research includes a comprehensive breakdown of RQ-20 power utilization and aircraft performance based on a combination of laboratory bench tests, flight data collection, and novel analysis techniques. We used this breakdown to generate a model of aircraft power consumption that accurately predicts the typical flight endurance observed today in operational environments. Building on this aircraft model, we determined the performance of a PV array through various flight maneuvers. We additionally incorporated a detailed solar insolation model to provide the greatest possible accuracy in our results.

We conclude that incorporating PV cells on the upper wing of the RQ-20 Puma significantly increases endurance during daytime flight operations. There are moderate but still significant benefits during morning or afternoon flights in our worst-case environment and immense benefits that more than double potential flight endurance flying mid-day or in favorable environments. We additionally identified two specific potential changes or optimizations to flight TTPs or AV control algorithms that further improve endurance on an order of magnitude similar to what is possible with the addition of a PV array. Together, the integration of a PV array on an optimized aircraft has the potential to improve flight endurance in favorable environments from two to over twelve hours. All of these gains are possible through relatively low-cost commercially available hardware.

The benefits of increased flight endurance are even more dramatic when considering what the end-user ultimately needs from the aircraft—time over an objective and not just total flight time. The portion of a sortie spent in transit to an objective area at

relatively slow speeds is often of little value to the system operator. This "tax" must also be paid when the aircraft returns, further reducing the available time a system can be employed over a target where it is needed. The increase in flight endurance from a PV array, therefore, has an even more profound impact on the percentage of usable flight time the aircraft can remain over its target. Reducing the frequency of landings for battery replacement also reduces wear and tear on a platform that incurs significant abuse from these repetitive controlled crashes.

The benefits of increased endurance will have immediate impact on deployed forces and provide opportunities for even greater employment flexibility on missions that may not have even been possible or practical previously. In just one example, reconnaissance and special operations forces will be able to fully utilize the system while maintaining a low profile by eliminating the risk of exposure from recovering and launching SUAS every few hours for battery replacement.

A future operating environment characterized by small, light, and mobile units distributed across a wide battlespace with limited logistics could use the PV array of this system to power or recharge other electronics on the ground when the AV is not in use, making the system much more versatile beyond its primary function. This improvement serves to lighten the burden of batteries or other power sources needed by a warfighter in an austere environment and ties in with concepts of future warfare and expeditionary operations envisioned by the Marine Corps.

## B. FUTURE WORK

The most surprising finding of this research is that the RQ-20 does not currently appear to operate in the most battery-efficient manner during normal flight operations. Even though the aircraft appears to have been designed to be flown in "far range" or "long endurance" modes, those specific speeds or algorithms are not specified in the operator's manual [15]. The only cruise speed specified (12 m/s) is consistent with an observed cruise speed of 13 m/s and does not appear to be an optimal speed from our analysis. Additional investigation of power consumption and aircraft performance in a regimen of manual flight modes should provide greater focus to these findings.

Some power utilization calculations used in this research were based on our best approximation and similarities between the RQ-11 and RQ-20 systems. This was due to not having access to a full RQ-20 fuselage on which we could disassemble subcomponents for precise measurements. A direct measurement of the entire RQ-20 system is preferred and may be possible in the future when hardware subcomponents are available for disassembly and more detailed research. It may be possible to revise total avionics subassembly and transmitter power from 12.0 W based on more precise measurements. Since most current missions are also conducted at a distance much less than the advertised 20 km maximum range, it is possible that adjustments could be made to the aircraft's transmitter power for significant power savings. There is no indication in current literature on the RQ-20 or testing on the RQ-11 that either platform has the ability to dynamically adjust power to minimize probability of intercept or to save battery consumption when maximum power is not necessary. Transmitter power may be further reduced if the aircraft, while airborne, can be placed into a mode that transmits flight data and video updates less frequently during transit or less critical phases of flight.

Our incorporation of a more detailed solar insolation model also revealed that a moderate amount of solar energy is available via diffuse irradiance in all environments. As a percentage of total irradiance, the diffuse portion is greatest at low sun elevations, or when total irradiance is also the lowest. It is possible that additional PV panels mounted on the underside of the wing or the sides and bottom of the fuselage could provide enough supplemental power to justify the additional cost and weight of hardware. A key component of weight is the added MPPT for each panel; a lighter or application specific MPPT would reduce this burden.

Our analysis of the impact of PV cells on flight performance mainly focused on present TTPs, flight procedures, or methods of employment. For example, the only type of maneuver analyzed was the circular level turn currently used by the aircraft in automatic flight modes. It is possible that an aircraft equipped with a PV array would benefit from other orbit geometries that try to maximize time spent with an array facing the sun and minimize time in other orientations.

Further modifications to this or other SUAS platforms could incorporate a smaller and lighter battery, relying primarily on the PV array for power, using the weight savings for heavier or more capable payload options. The addition of a PV array on larger group 4/5 UAS can provide a supplemental or backup source of power for payloads, aircraft systems, and more complex electronics. Future replacement group 1 platforms developed to fill small unit mission requirements should incorporate PV considerations as a design constraint. Aircraft of this class are typically optimized with long, narrow wings for other aerodynamic reasons. Incorporating the benefits of a PV system in the design stage may lead to an optimization of aircraft with a larger wing area to support more PV cells for even longer daytime flight endurance.

# LIST OF REFERENCES


[1] Department of Defense, “Unmanned systems integrated roadmap FY2013-2038,” DoD, Reference Number 14-S-0553, Washington, DC, 2013.

[2] U.S. Marine Corps, “2018 Marine Aviation Plan,” Department of Defense, Washington, DC, 2018.

[3] J. M. Pickup, (Capt.), interview, 6 March 2018.

[4] C. R. Gromadski, “Extending the endurance of small unmanned aerial vehicles using advanced flexible solar cells,” M.S. thesis, ECE Dept., Naval Postgraduate School, Monterey, CA, 2012.

[5] Marine Corps Expeditionary Energy Office, “Initial Capabilities Document for United States Marine Corps Expeditionary Energy, Water, and Waste,” Department of Defense, Washington, DC, 2011.

[6] W. R. Hurd, “Application of copper indium gallium diselenide photovoltaic cells to extend the endurance and capabilities of unmanned aerial vehicles,” M.S. thesis, ECE Dept., Naval Postgraduate School, Monterey, CA, 2009.

[7] J. V. Coba, “Application of copper indium gallium diselenide photovoltaic cells to extend the endurance and capabilities of the Raven RQ-11B unmanned aerial vehicle,” M.S. thesis, ECE Dept., Naval Postgraduate School, Monterey, CA, 2010.

[8] C. K. Chin, “Extending the endurance, missions and capabilities for most UAVs, using advanced flexible/ridged solar cells and using new high power density batteries technology,” M.S. thesis, ECE Dept., Naval Postgraduate School, Monterey, CA, 2011.

[9] S. B. Carey, “Increasing the endurance and payload capacity of unmanned aerial vehicles with thin-film photovoltaics,” M.S. thesis, ECE Dept., Naval Postgraduate School, Monterey, CA, 2014.

[10] M. D. Lai, “Application of thin film photovoltaic CIGS cells to extend the endurance of small unmanned aerial systems,” M.S. thesis, ECE Dept., Naval Postgraduate School, Monterey, CA, 2017.

[11] N. Camacho, “Improving operational effectiveness of tactical long endurance unmanned aerial systems (TALEUAS) by utilizing solar power,” M.S. thesis, MAE Dept., Naval Postgraduate School, Monterey, CA, 2014.

[12] D. J. Edwards, A. D. Kahn, M. Kelly, S. Heinzen, D. A. Scheiman, P. Jenkins, R. Walters and R. Hoheisel, “Maximizing net power in circular turns for solar and autonomous soaring aircraft,” *Journal of Aircraft,* vol. 53, no. 5, 2016.

[13] AeroVironment, “Puma AE RQ-20B Datasheet,” AeroVironment, Inc., Monrovia, CA, 2017.

[14] MAG Aerospace, “RQ-20 Puma,” 2018. [Online]. Available: https://magaero.com/rq-20-puma/. [Accessed 2 April 2018].

[15] AeroVironment, Inc., “Small Unmanned Aircraft System (SUAS) Puma AE II with Digital Data Link Operator’s Manual,” AeroVironment, Inc., Monrovia, CA, 2015.

[16] S. Michael, *Solar Cells Presentation, EC3230 Space Power and Radiation Effects,* Naval Postgraduate School, 2018.

[17] National Renewable Energy Laboratory, “Copper Indium Gallium Diselenide Solar Cells,” U.S. Department of Enervy, [Online]. Available: https://www.nrel.gov/pv/copper-indium-gallium-diselenide-solar-cells.html. [Accessed 29 May 2018].

[18] “Solar Power Planet Earth,” 2016. [Online]. Available: http://www.solarpowerplanetearth.com/solarpanels.html. [Accessed 30 March 2018].

[19] C. Frohlich and R. W. Brusa, “Solar Radiation and it Variation in Time,” *Solar Physics,* vol. 74, p. 209, 1981.

[20] W. B. Stine and M. Geyer, “Power From the Sun,” 2001. [Online]. Available: http://www.powerfromthesun.net/book.html. [Accessed 18 April 2018].

[21] Green Rhino Energy Ltd. , “Defining standard spectra for solar panels,” 2016. [Online]. Available: http://www.greenrhinoenergy.com/solar/radiation/ spectra.php. [Accessed 29 May 2018].

[22] D. J. Edwards, A. D. Kahn, M. Kelly, S. Heinzen, D. A. Scheiman, P. P. Jenkins, R. Walters and R. Hoheisel, “Maximizing Net Power in Circular Turns for Solar and Autonomous Soaring Aircraft,” *Journal of Aircraft,* vol. 53, no. 5, pp. 1237–1247, 2016.

[23] J. A. Duffie and W. A. Beckman, Solar Engineering of Thermal Processes, Hoboken, NJ: John Wiley & Sons, 2013.

[24] H. C. Hottel, “A Simple Model for Estimating the Transmittance of Direct Solar Radiation Through Clear Atmospheres,” *Solar Energy*, vol. 18, no. 2, pp. 129–134, 1976.

[25] J. S. Madren, “Optimized granularity analysis of maximum power point trackers in low power applications,” M.S. Thesis, ECE Dept., Naval Postgraduate School, Monterey, CA, 2017.

[26] Powersim, “Tutorial, Lithium-Ion Battery Model,” October 2016. [Online]. Available: https://powersimtech.com/drive/uploads/2016/12/Tutorial-Lithium-Ion-Battery-Model.pdf. [Accessed 11 July 1018].

[27] PowerStream, “How to calculate battery run-time,” PowerStream Technology, 17 November 2017. [Online]. Available: https://www.powerstream.com/battery-capacity-calculations.htm. [Accessed 11 July 2018].

[28] D. Ensenat, RQ-20 Puma depot-level maintenance, interview, 5 March 2018.

[29] “Raven RQ-11 Datasheet,” AeroVironment, Monrovia, CA, 2017.

[30] M. Smith, “Total Drag,” [Online]. Available: https://www.pilotwings.org/total-drag.html. [Accessed 15 July 2018].

[31] H. Estorga, RQ-20 Flight Operations, interview, 6 March 2018.

[32] Global Solar Energy, Inc., “FG-SM12-11: 8.3W (6V) Solar Submodule,” Global Solar Energy, Inc., Tuscon, AZ, 2015.

[33] Genasun, “MPPT Solar Controllers,” Blue Sky Energy, Vista, CA, 2017.

THIS PAGE INTENTIONALLY LEFT BLANK

# INITIAL DISTRIBUTION LIST

1. Defense Technical Information Center
   Ft. Belvoir, Virginia

2. Dudley Knox Library
   Naval Postgraduate School
   Monterey, California